Contents

Chapter 1

Introduction

1.1 Overview

The interest in the field of thermomechanics at the nanoscale has grown at a tremendous pace in the last decade, thanks to the availability of novel material processing and growth techniques and to the emergence of new detection methods. The interest is both scientific and technological.

The mechanics and thermal dynamics are expected to drastically change as objects dimensions shrink. Mode quantization, both bulk and surface, become important. Fluctuations in both sample dimensions and "environment" temperature start affecting the macroscopic response. The thermomechanical dynamics takes places on a time scale ranging from few picoseconds to tens of nanosecond and on sub-μm length scales. These scales question the applicability of theoretical frames so far applied to bulk systems and call for experiments providing fast-time resolution and low-perturbing sensitive probes.

Under an applicative standpoint, issues such as thermal management in nanoelectronic devices, thermomechanical responses in MicroElectroMechanical Systems (MEMS) and Opto-Acoustical devices in the hypersonic frequency range for both high resolution imaging and mass trafficking, just to mention a few, are of

paramount importance.

The present work stems from this context and focuses on surface-based phononic crystals as toy systems allowing to access, in conjunction with time-resolved ultrafast optics, both thermal and mechanical properties of nanosystems. These systems are periodic elastic composites of two or more vibrating materials, obtained patterning the surface of a substrate material either by metal deposition or substrate etching.

All-optical time-resolved experiments in a diffraction scheme, requiring a periodic optical lattice such as a surface phononic crystal, allow to deliver an energy density dU_V to the nanostructure. The same technique allows following, in the time domain, the energy relaxation dU_V from the nanostructure to the substrate, serving as an external bath. Both the thermal δQ_V and mechanical energy δW_V, branching from the absorbed total energy dU_V, can be followed. The optical probe, besides providing time-resolution, is a non-contact low-perturbing probe. This peculiarity is particularly important for detection of minute thermal fluxes and displacements fields.

As far as applications, assessing the role of geometry and material parameters of surface phononic crystals, with respect to surface wave generation, paves the way to the engineering of hypersonic surface acoustic waves generators and detectors beyond a trial-and-error approach. Surface-based phononic crystals, in conjunction with ultrafast optics, thus provide an ideal system to investigate both nanocalorimetry and nanomechanics and a valuable generation/detection scheme for hypersonic surface waves.

1.2 Outline

This work is organized as follows: in Chapter 2 we review the background and advances on ultrafast generation and detection of thermal gradients and pseu-

dosurface acoustic waves in two-dimensional lattices of metallic nanostructures. Comparing the experimental findings to the numeric analysis of the thermomechanical problem, these materials emerge as model systems to investigate both the mechanical and thermal energy transfer at the nanoscale.

In Chapter 3 we present a theoretical framework allowing to properly address the nature of surfacelike eigenmodes in a 2D hypersonic surface phononic crystal. An overall comprehension of this physics is still missing, due to the fact that there is no distinction between the eigenmodes of the surface-based nanostructures and the surface acoustic modes of the semi-infinite substrate, the solution of the elastic equation being a pseudosurface acoustic wave partially localized on the nanostructures and radiating energy into the bulk. This problem is solved by introducing a surface-likeness coefficient as a tool allowing to identify pseudosurface acoustic waves and to calculate their line shapes. Having accessed the pseudosurface modes of the composite structure, the same theoretical frame allows reporting on the gap opening in the now well-defined pseudo-SAW frequency spectrum. We show how the filling fraction, mass loading, and geometric factors affect both the frequency gap, and how the mechanical energy is scattered out of the surface waveguiding modes.

In Chapter 4 we explore the heat transfer δQ_V from the nanostructure to the substrate. That is the realm of nanocalorimetry. Over the last century calorimetry has been the method of choice for the investigation on thermodynamic properties of matter. Conventional calorimetry, however, is limited to sample sizes of few tens of micrograms. To overcome the downsizing limits of conventional calorimetry, we rely on all-optical time-resolved techniques. In this Chapter the thermal dynamics occurring in such experiments are theoretically investigated from 300 to 1.5 K. We report ab-initio calculations describing the temperature dependence of the electron-phonon interactions for Cu nanodisks supported on Si. The electrons and phonons temperatures are found to decouple on the ns time scale at ~ 10 K, which is two orders of magnitude in excess with respect to that found for standard

low-temperature transport experiments. Accounting for the physics behind these results, we suggest an alternative route for overhauling the present knowledge of the electron-phonon decoupling mechanisms in nanoscale systems by replacing the mK temperature requirements of conventional experiments with experiments in the time-domain.

In Chapter 5 the mechanical energy transfer δW_V from the nanostructure to the substrate is explored. We present a theoretical framework allowing to properly investigate the optical generation of pseudosurface acoustic waves in a hypersonic surface phononic crystal. Exploiting finite-elements analysis, together with the models developed in Chapters 3 and 4, we follow step by step in the time domain the initial impulsive heat-driven displacement launching pseudo-SAWs and evaluate their lifetime. We then test our approach against the results of time-resolved optical diffraction experiments performed on the same composite systems [1].

Chapter 2

State of the art

The use of femtosecond laser pulses to impulsively excite thermal and mechanical transients in matter has led, in the last years, to the development of picosecond acoustics. Recently, the pump-probe approach has been applied to nanoengineered materials to optically generate and detect acoustic waves in the GHz frequency range. In this Chapter, we review the background and advances on ultrafast generation and detection of thermal gradients and pseudosurface acoustic waves in two-dimensional lattices of metallic nanostructures. Comparing the experimental findings to the numeric analysis of the thermomechanical problem, these materials emerge as model systems to investigate both the mechanical and thermal energy transfer at the nanoscale.

2.1 Picosecond ultrasonics

The use of ultrafast laser pulses (pulse duration $\leq$ 1 ps) to generate and detect thermomechanical transients in matter opened the field of picoseconds ultrasonics [2]. The basic idea is to use sub-ps light pulses in a "percussion" approach, in which an intense pulse (pump), focused on an area A of a solid surface, impulsively delivers an energy dU within the light penetration depth Λ, inducing a non-equilibrium local heating of both electrons and lattice on the ps-timescale. The local temperature increase

$$\Delta T = [dU/(A\Lambda C)] \cdot e^{-z/\Lambda} \, , \tag{2.1}$$

with C as the specific heat per unit volume, is coupled to a sudden lattice expansion through the thermal expansion coefficient α. The photoinduced thermoelastic stress is able to launch strain pulses $\eta(z,t)$ propagating away from the excited surface along the direction z, regulated by [3]:

$$\eta\left(z,t\right) = \frac{dU\alpha}{A\Lambda C} \, \frac{1+\nu}{1-\nu} \, f\left(z-vt\right) \, , \tag{2.2}$$

ν being the Poisson ratio and $f\left(z-vt\right)$ the function describing the shape of the strain pulse, moving at the longitudinal sound velocity v. The dependence of the refractive index on the strain, through the photoelastic constant, allows to follow the propagation of strain pulses by means of a second delayed pulse (probe). An energy per pulse of the order of $dU \sim 1$ nJ, easily available by means of Ti:sapphire oscillators producing $\sim$ 120 fs light pulses, can be exploited to impulsively heat semiconductor or metal samples leading to temperature increase $\Delta T \sim 0.1 - 10$ K, implying thermoelastic stresses ranging from 0.1 to 1 Mbar.

The first evidences of picosecond acoustic transients in semiconductors and metals, reported in the seminal work by Maris et al. [3], triggered the investigation of the microscopic mechanisms responsible for the strain generation. At present, there is general agreement that, in semiconductors, the accumulation of the long-lived photo-injected excitations modifies the orbital population, inducing

an electronic stress coupled to an impulsive contraction or expansion of the lattice through the deformation potential [4]. This mechanism is always accompanied by the volume expansion related to the increase of the phonon population through the anharmonicity of the crystal potential. The latter effect, named lattice thermoelasticity, completely dominates in metals, where a rapid intraband relaxation of high-energy electrons is achieved by means of electron-phonon scattering. The temperature dynamics of the photoinduced non-equilibrium electrons and phonons in metals can be satisfactorily described by the two-temperature model (2TM) [5]. The main prediction is a local quasi-thermalization at an effective temperature T^* of electrons and phonons, on the timescale of $\sim$ 1 ps. The short thermalization time ensures that part of the energy dU of the pump pulse is efficiently converted into strain energy. This characteristic made very common the use of metal thin films as light-sound transducer to launch ultrasonic acoustic pulses in materials [6, 7].

The use of high-energy amplified Ti:sapphire oscillators opened the way to the investigation of the high-intensity strain regime, where the non-linear effects become effective. Pump pulses with energy of the order of $dU \sim 10-100$ nJ generate acoustic pulses with strain amplitude of the order of 10^{-3} and a time duration of the order of 10 ps. In this regime the balance between the increase of the sound velocity with strain and the decrease of the velocity of the high-frequency components of the strain pulse, due to the flattening of the phonon dispersion, results in the generation of sub-THz acoustic solitons, described by a Korteweg-de Vries equation [8]. After the first evidences of acoustic solitons generation in semiconductor and transparent media, solitons have been exploited to modulate the band gap of semiconductor quantum-wells, through the deformation potential [9].

When exciting samples at surfaces, a particular class of solutions of the elastic equation is constituted by surface acoustic waves (SAWs), i.e. acoustic waves confined at the surface within a depth of the order of their wavelength λ [10]. SAWs in the hypersonic frequency range ($\geq$ 1 GHz) are currently used to ma-

nipulate electrons in semiconductor devices [11, 12] and photons in microcavities [13, 14, 15]. The quest for efficient SAWs generation and detection techniques at ever higher frequencies led to the investigation of SAWs generation by means of ultrashort laser pulses. In particular, when the pump pulse is focused on a small area ($A \sim 1-10\ \mu m^2$) of a solid surface, the large Fourier spectrum allows launching SAWs at different k-wavevectors. Time-resolved imaging techniques have been employed to follow on the ps timescale SAW propagation on free surfaces [16, 17], through grain-boundaries [18], in phononic crystals [19] and in resonators [20].

The possibility to selectively excite bulk quasi-monochromatic acoustic waves became real by employing engineered materials with artificial periodicities of the elastic properties. In these systems, the pump pulse induces an impulsive strain with the wavelength matching the periodicity of the structure. The use of semiconductor superlattices allowed exciting coherent THz acoustic phonons via impulsive stimulated Raman scattering [21] and, only recently, to access the dynamics of hypersonic acoustic pulses confined into an acoustic nanocavities [22].

Parallel efforts have been devoted to the use of ultrafast light pulses to excite acoustic eigenmodes of confined nanostructures, after the first study of the vibrational modes of gold nanostripes on a fused quartz substrate [23]. Recently, advances in the preparation of quasi-monodispersed nanostructures enabled, employing picosecond ultrasonic techniques, to investigate photo-induced coherent oscillations in metallic nanoparticles [24, 25], nanocolums [26] and nanoprisms [27, 28, 29, 30], achieving optical control of the acoustic vibrations [31]. More recently, the feasibility of pump-probe measurements on single metallic nanoparticles [30], exploiting the surface plasmon resonance, opened the way to investigate the mechanical properties of single nanostructures, whose shape and interaction with the environment can be exactly determined by means of electron microscopy techniques [32].

2.2 Sub-nanosecond thermal transport

Notably, the same pump probe technique can be applied to study heat transport in matter [33]. The pump-induced ΔT triggers a heat flow on the sub-ns timescale. The dependence of the refractive index on the temperature enables following the propagation of heat pulses by means of the probe pulse. This technique, named time-domain thermoreflectance, has been employed to investigate the thermal conductance at metal-metal [34] and metal-dielectric [33, 35] interfaces and to disentangle the energy transport related to electron diffusion [34], anharmonic phonon decay [35] and ballistic phonon transport [36]. Recently, the signature of ballistic heat transport [37], at cryogenic temperatures, has been reported for a GaAs crystal covered by a metallic thin film transducer [38]. The extension of this technique to the study of thermal transport between a single metallic nanoparticle and the environment is a more difficult task, due to the difficulties in controlling the properties of the nanoparticle-environment interface [39].

The frontier in this intriguing research field is the investigation of the thermomechanical transients in lattices of metallic nanostructures on surfaces [23, 40, 1, 41, 42]. State of the art nanolithography and patterning techniques allow obtaining metallic nanostructures, whose shapes, dimensions, periodicities and interface properties can be carefully tuned. The interest in these systems is inherent to the following features: i) the periodicity, scalable down to $\sim$ 50 nm [43], that can be exploited to launch quasi-monochromatic SAWs in the substrate at $\sim$ 100 GHz [44]; ii) the periodicity of the elastic properties, that induces the opening of a band gap in the acoustic modes (hypersonic phononic crystals) [45]; iii) the fine control over the nanostructures-substrate interface, mandatory to study heat transport at the nanoscale.

Chapter 3

Pseudosurface acoustic waves in hypersonic surface phononic crystals

We present a theoretical framework allowing to properly address the nature of surfacelike eigenmodes in a hypersonic surface phononic crystal, a composite structure made of periodic metal stripes of nanometer size and periodicity of 1 μm, deposited over a semi-infinite silicon substrate. An overall comprehension of this physics is still missing, due to the fact that there is no distinction between the eigenmodes of the surface-based nanostructures and the surface acoustic modes of the semi-infinite substrate, the solution of the elastic equation being a pseudosurface acoustic wave partially localized on the nanostructures and radiating energy into the bulk. This problem is particularly severe in the hypersonic frequency-range, where semi-infinite substrate's surface acoustic modes strongly couple to the periodic overlayer, thus preventing any perturbative approach. The problem is solved by introducing a surface-likeness coefficient as a tool allowing to identify pseudosurface acoustic waves and to calculate their line shapes. Having accessed the pseudosurface modes of the composite structure, the same theoretical frame al-

lows reporting on the gap opening in the now well-defined pseudo-SAW frequency spectrum. We show how the filling fraction, mass loading, and geometric factors affect both the frequency gap, and how the mechanical energy is scattered out of the surface waveguiding modes.

3.1 Introduction

The idea of creating solids with artificial modulation in their physical parameters [46] has proved fruitful both in the frame of coherent electronic transport and photonics [47, 48] with the advent of semiconductor superlattices and photonic crystals [49, 50, 51], respectively. The analogy between photons and phonons suggested considering phononic crystals [52], periodic elastic composites of two or more vibrating materials, the interest being triggered by the possibility of achieving a frequency gap in the elastic modes dispersion relations and the wealth of applications stemming from tailoring the gap itself.

Extensive investigation of acoustic band structures of periodic elastic composite has been carried out on two-dimensional (2D) phononic crystals both infinite [52] and surface terminated [53, 54]. The archetypal 2D structure consists of parallel rods embedded in an elastic background. Rods can be actual or virtual ones (drilled holes). In the real case of a surface-terminated phononic crystal, an interesting class of acoustic modes, addressed as surface acoustic waves (SAWs) (arising from breaking of the translational symmetry when passing from an infinite to a semi-infinite medium) propagate confined to the elastic medium surface, the penetration depth being on the order of their spatial period. Recent works elucidated some of the characteristics of surface acoustic waves in 2D phononic crystals of different geometrical configurations [55, 56, 57, 58].

The present Chapter focuses on pseudosurface acoustic modes, reminiscent of surface acoustic waves, in surface-based phononic crystals. These structures are obtained patterning the surface of a substrate material either by metal deposition or substrate etching. The influence of a periodically structured overlayer on the acoustic-field eigenmodes of a thick or thin homogeneous slab has been studied by many research groups and effects such as band folding [59, 60], mode leakage [61], opening of frequency gaps [19, 59, 60, 61, 62, 63], and interaction between slab and overlayer modes [63, 64, 65] have been discussed. Contrary to 2D phononic

crystals, for surface acoustic modes in surface-based phononic crystals there is no distinction between the eigenmodes of the nanostructures and SAWs, the solution of the elastic equation being a pseudosurface acoustic wave partially localized on the nanostructures and radiating energy into the bulk. This issue is particularly severe in the hypersonic frequency range, where the semi-infinite substrate's surface acoustic modes strongly couple to the periodic overlayer, thus preventing any perturbative approach. In this physical scenario, we present a theoretical framework allowing to properly address the nature of surfacelike eigenmodes in a hypersonic surface phononic crystal. We solve the problem introducing a surface-likeness coefficient as a tool allowing to find pseudosurface acoustic waves and to calculate their line shapes. Having accessed the pseudosurface modes of the composite structure, the same theoretical frame allows reporting on the gap opening in the now well-defined pseudo-SAW frequency spectrum. We show how the filling fraction, mass loading, and geometric factors affect both the frequency gap, and how the mechanical energy is scattered out of the surface waveguiding modes.

These results are of interest also from an applicative stand point. The quest for hypersonic acoustic waveguides [66], sources of ultrafast coherent acoustic waves and nano-optoacoustic transducers in general, operating at ever higher frequencies, requires patterning periodic structures of ever decreasing periodicities. In this frame, surface-based phononic crystals provide a technological advantage over 2D phononic ones, the processing technique involving the surface only, being easily scalable below 100 nm and suitable for high-frequency transducers technology. The theoretical tool here presented, together with the comprehension of how the construction parameters affect the frequency gap and surface waveguiding mode, will be a valuable tool for inspecting the pseudo-acoustic modes relevant for applications in view of device engineering beyond a trial-and-error approach.

This Chapter is organized as follows: in Section 3.2 we outline and solve the full mechanical problem, calculating the vibrational normal modes of the composite system. The presence of periodic nickel stripes modifies the properties of surface

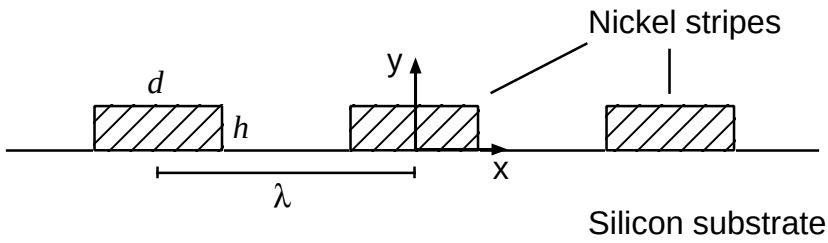

FIGURE 3.1: Schematic diagram of the surface phononic crystal. Isotropic nickel stripes of width d and height h are deposited on a crystalline silicon substrate. The grating has period λ. Propagation direction is along the x axis, surface normal to the bulk is along the y axis.

waves [10, 67, 68]. The SAW is no longer an eigenmode of the elastic eigenvalue problem. Proper assessment of a pseudo-SAW in a surface-based phononic crystal is achieved in Section 3.3. We introduce a SAW-likeness coefficient permitting to discriminate pseudo-SAWs among the entire set of eigenmodes. Investigation of the gap opening in a surface-based phononic crystal as a function of the filling fraction p, beyond a perturbative approach, is presented in Section 3.4. We show how the frequency gap depends on the set of geometric factors $\{p, h\}$ and mass loading $\{m, \rho\}$ - m, ρ and h being the nickel stripe's mass, density and height, respectively. In Section 3.5 we analyze the energy distribution in the system as a function of p and relate it to the scattering of SAWs into the bulk.

3.2 Mechanical model

We assume the system to be an elastic continuum composed of a periodic metallic grating deposited on a silicon substrate. In Fig. 3.1, we consider the general configuration where elastic isotropic nickel stripes of width d and height $h = 50$ nm are deposited on a crystalline silicon substrate. The grating has period $\lambda = 1$ μm, thus ensuring pseudo-SAWs in the hypersonic range. Calculations are performed increasing d, in order to cover the entire filling fraction p range $(0, 1)$, where $p =$

TABLE 3.1: Material properties for Si substrate (Ref. [70]) and Ni stripes (Ref. [71]): Young's modulus E, Poisson's ratio σ, and mass density ρ.

	E (GPa)	σ	ρ (Kg/m^3)
Si substrate	131	0.27	2330
Ni stripes	219	0.31	8900

d/λ, and explore different regimes, from a perturbative one ($p \ll 1$) to substrate full coverage ($p = 1$). The acoustic equation of motion governing the displacement $\mathbf{u}(\mathbf{r}, t)$ of the composite system is

$$\partial_j \left[c_{ijmn} \left(\mathbf{r} \right) \partial_n u_m \right] = \rho \left(\mathbf{r} \right) \ddot{u}_i \ , \tag{3.1}$$

where $\rho \left(\mathbf{r} \right)$ and $c_{ijmn} \left(\mathbf{r} \right)$ are the position-dependent mass density and elastic stiffness tensor, respectively, and the summation convention over repeated indices is assumed. For an harmonic time dependence $e^{i\omega t} + c.c.$, Eq. 3.1 reads

$$\partial_j \left[c_{ijmn} \left(\mathbf{r} \right) \partial_n u_m \right] = -\rho \left(\mathbf{r} \right) \omega^2 u_i \ . \tag{3.2}$$

The eigenvalue problem is solved via the finite-elements method [69]. As shown in Fig. 3.2(a), the model consists of a two-dimensional silicon rectangular cell with a nickel stripe on top. The material properties for the silicon substrate and the nickel stripes, that enter in the expression of the elastic stiffness tensor, are reported in Table 3.1. The silicon substrate's crystalline orientation is accounted for in the expression of the elastic stiffness tensor and, in the present case, the x axis is taken along the Si(100) crystalline direction. To reproduce the entire nanostructured composite from the single unit cell, the displacements $\mathbf{u}_1$ and $\mathbf{u}_2$, calculated, respectively, on side 1 and 2 of the cell [see Fig. 3.2(a)], are related by $\mathbf{u}_1 = e^{iK_{x,n}\lambda} \, \mathbf{u}_2$, as required by the Bloch theorem, where $K_{x,n} = k_x + 2\pi n/\lambda$ and $k_x \in (-\pi/\lambda, \ \pi/\lambda)$. The displacement is fixed to zero on the base boundary

and the height L of the cell is set to 100 μm, two orders of magnitude greater than the system's periodicity. This condition is required to achieve a density of states fine enough to appreciate the surface-confined system's normal modes also for $p \ll 1$ and $p \sim 1$, the eigenfrequencies spacing scaling as $1/L$. Attention is devoted in choosing the finesse of the quadratic-ordered mesh, enabling accurate displacements calculations despite: i) the size discrepancy between the nanostructure and the silicon cell; ii) the two orders of magnitude difference between L and λ. Unless otherwise stated, the calculations are performed with $n = 1$ and $k_x = 0$ ($K_{x,1} = 2\pi/\lambda$), corresponding to the first harmonic at the center of the surface Brillouin zone, calculation of the eigenfrequencies as a function of the wave vector parallel to the surface of the substrate not being the main scope of this work.

3.3 Pseudo-SAW

On the contrary to bulk modes, SAWs are confined in a thin layer starting at the surface of the substrate. As seen in Fig. 3.2(b), in the case of a pure silicon slab, without stripes on top, the displacement field vanishes within a depth on the order of 1 μm, i.e. of the SAW wavelength, corresponding to the chosen grating period λ. The total displacement color scale normalized over its maximum value is reported, together with the displacement field. These modes are the elastic analogs of the electronic surface states [72] or the electromagnetic evanescent waves encountered at the surface of a semi-infinite solid [73]. The surface wave is an exact solution of the eigenvalue problem, twofold degenerate under translational symmetry. The two solutions $\mathbf{u}_u$ and $\mathbf{u}_g$ have, respectively, sin (*ungerade*) and cos (*gerade*) symmetry. In Fig. 3.2(b) only the sin symmetry solution is reported. The calculation of the twofold-degenerate eigenfrequency at the Brillouin-zone center ($n = 1$) gives $\tilde{\nu} = 4.92$ GHz, in agreement with data for a SAW propagating along Si(100) [67].

On a uniform flat surface a surface wave does not radiate into the bulk and has

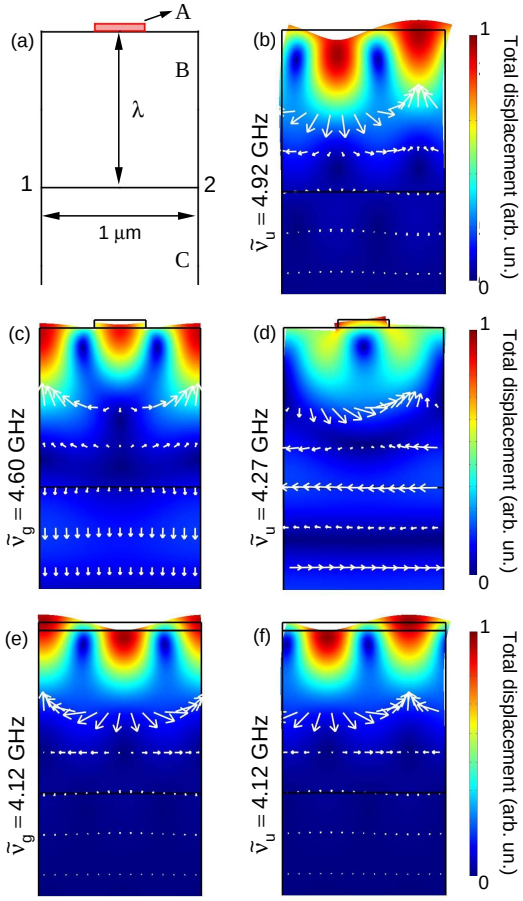

FIGURE 3.2: Nickel stripe on silicon substrate. (a) The top 2 μm portion of the 2D rectangular unit cell is reported. The cell geometry is divided in three parts: A. Ni stripe, B. 1 μm top portion of Si substrate, C. 99-μm-thick Si bulk portion. Bloch boundary conditions are set on sides 1 and 2 of the substrate. The periodicity is $\lambda = 1$ μm. The height of the Si cell is 100 μm. The Ni stripe is $h = 50$ nm high and, in this figure, $d = 320$ nm wide. In figures (b) trough (f), the deformation and arrows correspond to the displacement field, while the color scale refers to the normalized total displacement. (b) Sin-like SAW solution for a pure silicon slab. The orthogonal cos-like eigenfrequency degenerate solution is not reported. (c) Cos-like and (d) sin-like pseudo-SAW solutions for $d = 320$ nm. (e) Cos-like and (f) sin-like SAW eigenfrequency degenerate solutions for substrate full coverage.

a penetration depth $\sim \lambda$ [10]. The presence of periodic nanostructures is expected to modify the properties of the SAW, perturbing the stress and velocity fields associated with SAW propagation [23, 1, 74]. In the periodic composite system the SAW modes are not solutions of the eigenvalue problem. The eigenmodes of the full structure, whose displacement field most closely resemble the unperturbed SAWs, are shown in Figs. 3.2(c) and 3.2(d). The twofold degeneracy is lifted and a band gap opens: one mode, with sin symmetry, is found at $\tilde{\nu}_u = 4.27$ GHz, whereas a second mode, with cos symmetry, is found at $\tilde{\nu}_g = 4.60$ GHz. The calculated displacement field is Rayleigh-type in region B, evident from the alike displacement fields of sin-like solutions in region B of Figs. 3.2(b), 3.2(d) and 3.2(f), and bulk-like in region C, clear from the field distribution in region C of Figs. 3.2(c) and 3.2(d). We address these modes as pseudo-SAWs. Periodic nanostructures force the previously unperturbed surface waves to radiate elastic energy into the bulk. The analog in the electromagnetic case is diffraction of surface plasmons into far field by a periodic metallic grating deposited on the substrate surface. In the acoustic case, the stress at the Ni-Si interface, needed to force the stripes to follow the motion of the surface, acts as the source of energy radiation into the bulk, as explained by Lin et al. [23]. In terms of scattering of unperturbed SAWs, this effect can be rationalized as the coupling of free-surface modes to the silicon bulk modes.

The eigenmodes for the case of full substrate coverage ($p = 1$) are reported in Figs. 3.2(e) and 3.2(f). The band gap closes, the degeneracy is recovered with $\tilde{\nu} = 4.12$ GHz, and the eigenvectors are SAWs, hence no energy is radiated in the bulk. The solution is similar to that reported in Fig. 3.2(b) for $p = 0$; the overlay downshifts the value of $\tilde{\nu}$.

In the previous discussion, the concept of pseudo-SAW was suggested on the basis of similarities between its displacement field and that of a pure SAW. Nevertheless the theory lacks a formal definition for a pseudo-SAW or a procedure allowing to spot out such solutions from the infinite eigenvalues set satisfying Eq. 3.2,

in the present geometry. With this aim in mind, the SAW-likeness coefficient is defined as

$$\alpha(\nu) \doteq \frac{\langle E_A(\nu)\rangle + \langle E_B(\nu)\rangle}{\langle E_{tot}(\nu)\rangle} \,, \tag{3.3}$$

where $\langle E_A(\nu)\rangle$, $\langle E_B(\nu)\rangle$, and $\langle E_{tot}(\nu)\rangle$ are the time-averaged mechanical energy contents of $\mathbf{u}(\mathbf{r})$ in region A, B, and in the entire unit cell, respectively [see Fig. 3.2(a)]. The calculation is here performed starting from $\mathbf{u}(\mathbf{r})$,

$$\alpha(\nu) = \frac{\int_A \rho(\mathbf{r})\,\mathbf{u}^2(\mathbf{r})d^3\mathbf{r} + \int_B \rho(\mathbf{r})\,\mathbf{u}^2(\mathbf{r})d^3\mathbf{r}}{\int_{tot} \rho(\mathbf{r})\,\mathbf{u}^2(\mathbf{r})d^3\mathbf{r}} \,. \tag{3.4}$$

The SAW-likeness coefficient $\alpha(\nu)$ outlines which eigenmodes of the system have mechanical energy mainly localized within a depth λ (where λ is both the nanostructure's period and the penetration depth of an unperturbed SAW of the same wavelength). In Fig. 3.3, we report $\alpha(\nu)$ for three values of p. Two distributions, $\alpha_g(\nu)$ and $\alpha_u(\nu)$, emerge from the plot, corresponding to the cos-like and sin-like displacement profiles, respectively. We define pseudo-SAWs the eigenmodes with frequencies $\tilde{\nu}_g$ and $\tilde{\nu}_u$, corresponding to the two distributions' maxima. The pseudo-SAWs are the solutions that most likely resemble the unperturbed SAWs. The eigenfrequency degeneracy is removed and the opening of a frequency band gap is directly shown. We pinpoint that the SAW-likeness coefficient is easily interpreted as the SAW line shape, the line shape concept arising because, in the composite system, the SAW is not an eigenmode. A more correct definition of SAW line shape and its relative linewidth will be given in Section 5.4.

In Fig. 3.3(a) the calculation for a sample with $p = 0.1$ ($d = 100$ nm) is reported. For small filling fractions, nickel stripes act as a weak perturbation to the modes of the underlying substrate. The values of the pseudo-SAW frequencies and the corresponding SAW-likeness coefficients, as well as the linewidth γ [full width at half maximum (FWHM)] of the two distributions, are reported in Table 3.2. The fact that $\alpha_g(\tilde{\nu}_g) > \alpha_u(\tilde{\nu}_u)$ means that the grating affects the sin-like SAW more than the cos-like one. Furthermore, the grating couples the unperturbed sin-like SAW over a wider range of modes: $\gamma_u > \gamma_g$. The frequency gap is

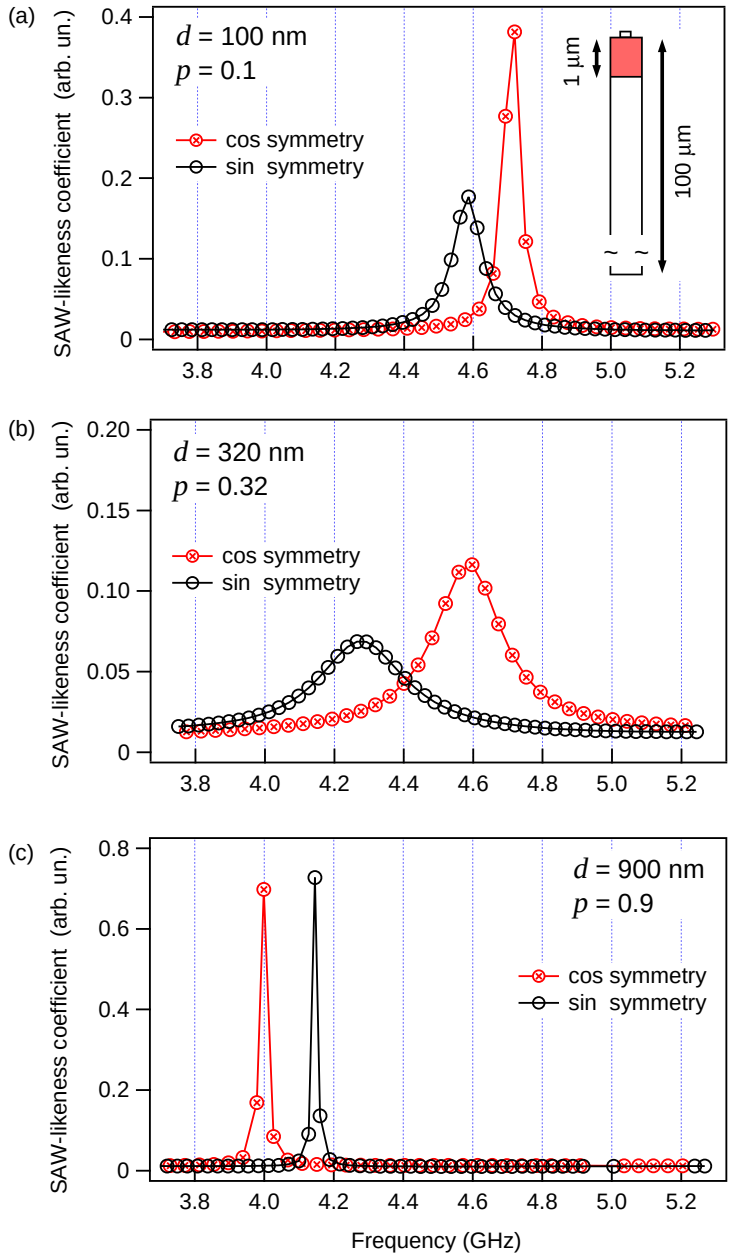

FIGURE 3.3: SAW-likeness coefficient $\alpha(\nu)$ versus the calculated eigenfrequencies. Two distributions arise, $\alpha_u(\nu)$ and $\alpha_g(\nu)$, corresponding to sin-like (empty circles) and cos-like (crossed circles) displacement profiles. Calculation for configurations with different filling fraction are reported: (a) $p = 0.1$, (b) $p = 0.32$, and (c) $p = 0.9$. Solid lines are intended as a guide to the eye.

TABLE 3.2: Calculated pseudo-SAW frequencies, corresponding SAW-likeness coefficients, and linewidth γ (FWHM) for both *gerade* and *ungerade* distributions.

p	0.1	0.32	0.9
$\tilde{\nu}_g$ (GHz)	4.72	4.60	4.00
$\alpha_g\,(\tilde{\nu}_g)$	0.38	0.12	0.70
γ_g (GHz)	0.064	0.231	0.013
$\tilde{\nu}_u$ (GHz)	4.59	4.27	4.15
$\alpha_u\,(\tilde{\nu}_u)$	0.18	0.07	0.73
γ_u (GHz)	0.101	0.300	0.010

$\Delta\tilde{\nu} = \tilde{\nu}_g - \tilde{\nu}_u = 0.13$ GHz. Both $\tilde{\nu}_g$ and $\tilde{\nu}_u$ are lower than the unperturbed SAW eigenfrequency $\tilde{\nu} = 4.92$ GHz.

Increasing the filling fraction to $p = 0.32$, we obtain the distributions reported in Fig. 3.3(b). The physics is now well beyond the perturbative approach: larger linewidths and lower values of the SAW-likeness coefficient for the two pseudo-SAWs are the signatures of a stronger SAW-stripes interaction, as compared to the case of $p = 0.1$. This leads to a higher coupling of surface waves with the bulk modes of the system, a confirmation to the evidence given in Figs. 3.2(c) and 3.2(d). The frequency gap is $\Delta\tilde{\nu} = 0.33$ GHz. Both $\tilde{\nu}_g$ and $\tilde{\nu}_u$ are further downshifted with respect to $\tilde{\nu}$. The pseudo-SAW frequency lowering is strongly dependent on the displacement field symmetry.

Increasing the filling fraction to $p = 0.9$, close to the silicon full coverage [see Fig. 3.3(c)], narrow linewidths and high peaked distributions resemble the frequency twofold-degenerate surface wave solutions shown for $p = 1$ in Figs. 3.2(e) and 3.2(f), consistently with a reduced frequency gap $\Delta\tilde{\nu} = -0.15$ GHz. Interestingly $\Delta\tilde{\nu}$ changes sign and the *ungerade* pseudo-SAW is now less affected by the periodicity as compared to its *gerade* counterpart. For the case of $p = 1$, $\tilde{\nu}$ is in

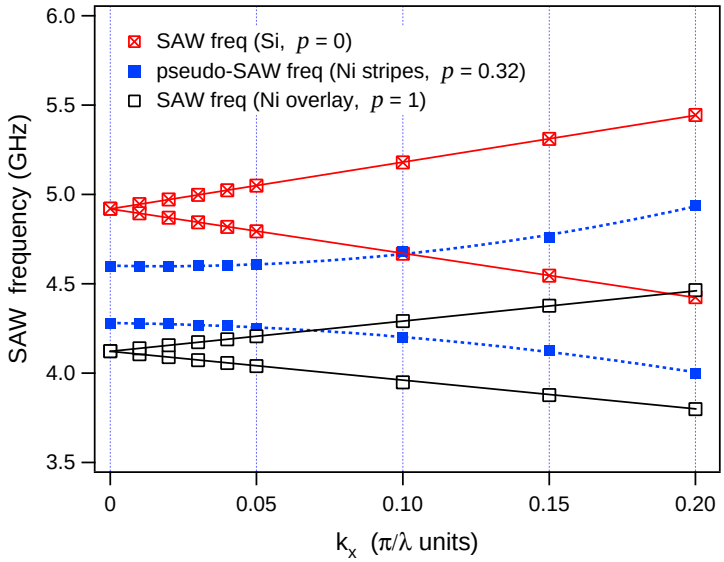

FIGURE 3.4: Dispersion relations of the elastic surface modes for small values of k_x (in π/λ units) and $n = 1$, for a pure silicon slab ($p = 0$), for silicon full coverage ($p = 1$) and for the configuration with Ni stripes over Si substrate ($p = 0.32$). Solid lines are fits to data. Dotted lines are a guide to the eye.

agreement with the analytical theory developed by B. Auld [67].

To further test the soundness of the pseudo-SAW definition adopted in the present work, we calculated for p= 0, 0.32, and 1, the dispersion for the first harmonic pseudo-SAW modes: $k_x \in [-0.2\pi/\lambda,\ 0.2\pi/\lambda]$ and $n = 1$. The outcome is shown in Fig. 3.4. The dispersion relation for the semi-infinite silicon slab ($p = 0$) starts at $\nu = 4.92$ GHz and is linear with a slope $v_s = 4900$ m/s, in agreement with the speed of sound reported for SAW on Si(100) [67]. For the full overlay case ($p = 1$), the dispersion starts at 4.12 GHz. Both solutions are true SAW eigenmodes of the system. For the case of $p = 0.32$, a gap opening is observed and the two dispersion branches for the pseudo-SAWs remain correctly confined between their $p = 0$ and $p = 1$ analogs.

3.4 Frequency gap

Having formally defined the pseudo-SAW, we now address the issue of the frequency gap in the pseudo-SAW modes. In Fig. 3.5 the pseudo-SAW frequencies and band gap calculated over the entire filling fraction range are shown. For $p \neq 0$, the pure silicon slab eigenfrequency degeneracy is lifted. As p increases, $\tilde{\nu}_g$ decreases until it reaches a plateau for $p = 0.2$. The plateau lasts for $p \in (0.2,\ 0.5)$ then, for $p > 0.5$, $\tilde{\nu}_g$ decreases monotonically till it jumps back to the SAW value for full coverage as soon as the stripes' width d reaches the size of the periodicity, becoming a complete overlay. There is a geometrical explanation for the discontinuity [see inset of Fig. 3.5]. For $p = 1$, periodic boundary conditions become effective also on the stripe's sides, the cos-like pseudo-SAW solution $\mathbf{u}_g$ undergoes a transition from free to constrained displacement on the stripe's lateral boundaries. The same constraints do not affect $\mathbf{u}_u$ because they are set where the nodes of the sin-like solution are found [see Fig. 3.2(f)]. In an experiment, for the above mentioned discontinuity, a steep positive derivative $\partial\tilde{\nu}_g/\partial p$ for $p \to 1$ should be expected in place of an abrupt transition. Concerning $\tilde{\nu}_u$, it is a monotonically decreasing function of p. It decreases with a steep slope for $p < 0.3$. It then changes slope stabilizing to an almost constant value all the way to $p = 1$. For $p < 0.75$, $\tilde{\nu}_g > \tilde{\nu}_u$; at $p = 0.75$ the eigenvalues cross; for $p > 0.75$, $\tilde{\nu}_g < \tilde{\nu}_u$; degeneracy is recovered for $p = 1$. In summary, the frequency gap $\Delta\tilde{\nu}$ opens as soon as $p \neq 0$. The maximum value $\Delta\tilde{\nu} = 0.40$ GHz is attained when the silicon surface is close to half coverage. For higher filling fractions, the gap decreases to $\Delta\tilde{\nu} = 0$ for $p = 0.75$. For values of p in excess of 0.75, $\Delta\tilde{\nu} < 0$ and decreases till it makes an abrupt transition back to $\Delta\tilde{\nu} = 0$ for $p = 1$.

The present results also show the limits of applicability of the perturbative approach [58]. Within a perturbative scheme the relative frequency shift is proportional to the filling factor:

$$\frac{(\tilde{\nu}(p) - \tilde{\nu}(0))}{\tilde{\nu}(0)} \propto (\frac{h}{\lambda})p\ . \tag{3.5}$$

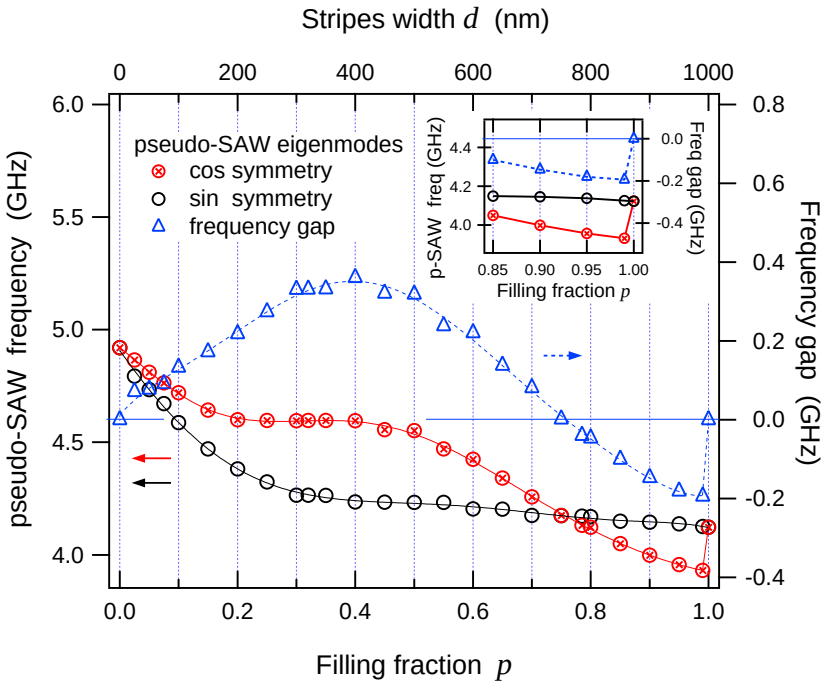

FIGURE 3.5: Left axis: pseudo-SAW eigenfrequencies $\tilde{\nu}_g$ (crossed circles) and $\tilde{\nu}_u$ (empty circles) versus surface filling fraction p (or stripes width d in nm, top axis). Right axis: pseudo-SAW frequency gap $\Delta\tilde{\nu}$ (triangles). The horizontal line is the $\Delta\tilde{\nu} = 0$ line and refers to right axis only. Inset: magnification of the graph for high filling fractions p is shown. Lines are a guide to the eye only.

Calculation of the relative frequency shift, on the basis of the results reported in Fig. 3.5, shows that linearity holds up to $p \sim 0.1$. For values of p in excess of 0.1 one has to rely on the full calculations here reported.

In the general case, for a fixed periodicity λ, the pseudo-SAW frequencies (both *gerade* and *ungerade*) are functions of the parameters $\{p, h, m, \rho\}$: $\tilde{\nu} = f(p, h, m, \rho)$. The four parameters are not mutually independent, being $\rho \propto m/(hp)$. $\tilde{\nu}$ is then defined in a four-dimensional space and it is a function of three parameters only, the fourth being fixed by the choice of the other three. For instance, each data point reported in Fig. 3.5 (left axis) is calculated having fixed p, h, and ρ independently. The plots are then obtained spanning p over the range $(0, 1)$, thus exploring a particular trajectory $\tilde{\nu}(p,\ h = 50$ nm, $\rho_{Ni})$ on the

hyper-surface $\tilde{\nu}(p, h, \rho)$. A full description is computationally too time consuming and would not add much to the comprehension of the physics without slicing the hypersurface along particular hyperplanes or trajectories.

To get a deeper physical inside, the effects on $\tilde{\nu}$ of the geometric factors $\{p, h\}$ and mass loading $\{m, \rho\}$, are here explored. We start considering a reference system configuration with $p = 0.2$, $h = 50$ nm, and $\rho = \rho_{Ni}$, hence the value of m is fixed to $m^{(ref)}$. The pseudo-SAW frequencies, calculated in the reference configuration, are $\tilde{\nu}_g^{(ref)}$ and $\tilde{\nu}_u^{(ref)}$. To test the contribution of the stripes' geometry, m and ρ are kept fixed at their reference values, while p is allowed to increase from 0.2 to 0.9. Doing so, the value h decreases. In Fig. 3.6(a) the dependences of $\tilde{\nu}_i - \tilde{\nu}_i^{(ref)}$ (with $i = \{g, u\}$) and $\Delta\tilde{\nu}$ on the geometric factor $\{p, h\}$ are shown. The geometric factor upshifts both frequencies, $\tilde{\nu}_u$ being more affected than $\tilde{\nu}_g$ and $\Delta\tilde{\nu}$ decreasing monotonically. The effect of the geometry in surface-based phononic crystal fits well with the results reported by Tanaka et al. [53] for a 2D phononic crystal in which no mass loading effect is to be expected (the band-gap definition is reversed in sign with respect to our case). This makes us confident that we are properly disentangling the geometry from mass loading effects. To inspect the mass loading effect, p and h are kept fixed at their reference values while ρ is raised up to 4.5 times the Ni density. Doing so, the value of m increases. In Fig. 3.6(b) the dependences of $\tilde{\nu}_i - \tilde{\nu}_i^{(ref)}$ and $\Delta\tilde{\nu}$ on the mass loading factor $\{m, \rho\}$ are shown. The mass loading downshifts both frequencies, $\tilde{\nu}_u$ being more affected than $\tilde{\nu}_g$ and $\Delta\tilde{\nu}$ increasing monotonically. The functions in Fig. 3.6(a) cannot be compared with the ones reported in Fig. 3.6(b) nor the absolute values are of relevance. The importance stands in the qualitative functions behavior, showing the disentangled physical effects of geometry and mass loading over $\tilde{\nu}_i$ and $\Delta\tilde{\nu}$. The present analysis shows that in a device the pseudo-SAW frequency gap results from a combination of geometry and mass loading factors, the two affecting the pseudo-SAW frequencies in opposite ways. A trade-off between p and m has to be foreseen for tailoring the pseudo-SAW frequencies or frequency gap in view of

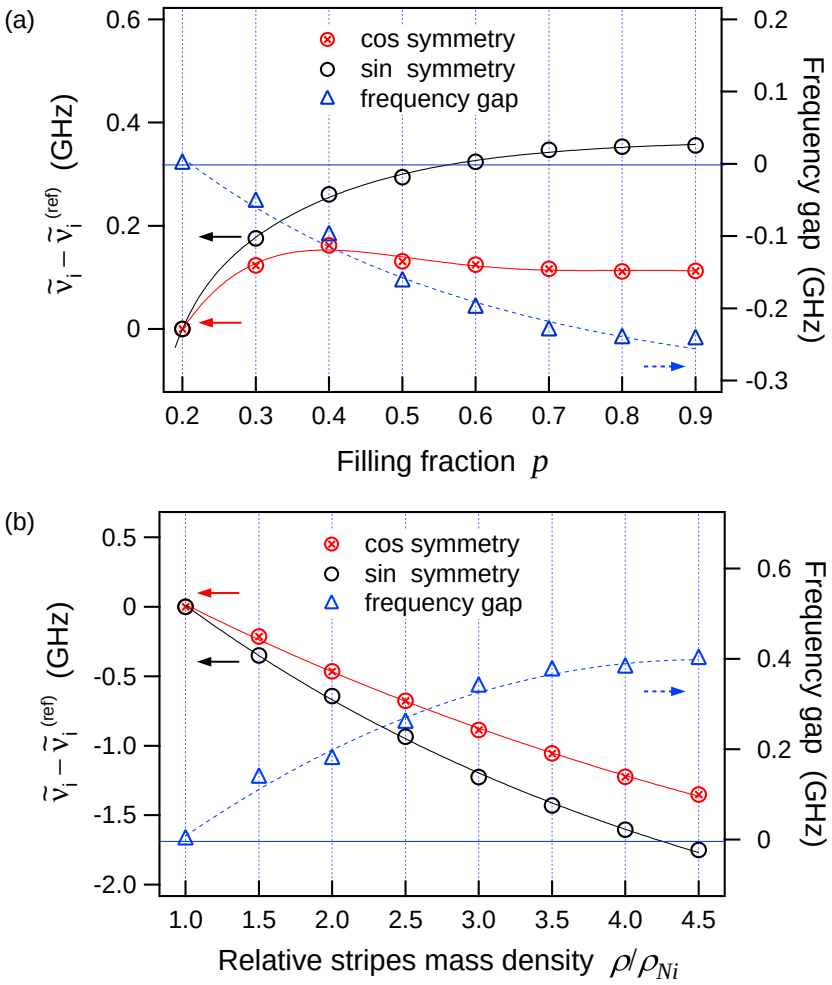

FIGURE 3.6: Geometric and mass loading effects on $\tilde{\nu}$. The reference system configuration is $p = 0.2$, $h = 50$ nm, and $\rho = \rho_{Ni}$, hence m is fixed to $m^{(ref)}$. The pseudo-SAW frequencies, calculated in the reference configuration, are $\tilde{\nu}_g^{(ref)}$ and $\tilde{\nu}_u^{(ref)}$. (a) Exploring the geometric effect: the mass loading factor $\{m, \rho\}$ is kept at the reference value, the variable being the geometric factor $\{p, h\}$. (b) Exploring the mass loading effect: the geometric factor $\{p, h\}$ is kept at the reference value, the variable being the mass loading factor $\{m, \rho\}$. Left axis: pseudo-SAW eigenfrequencies $\tilde{\nu}_g$ (crossed circles) and $\tilde{\nu}_u$ (empty circles). Right axis: pseudo-SAW frequency gap $\Delta\tilde{\nu}$ (triangles). The horizontal line is the $\Delta\tilde{\nu} = 0$ line and refers to right axis only. Lines are a guide to the eye only.

possible applications.

3.5 Mechanical energy radiation

In this Section, the energy distribution in the system, for both pseudo-SAW eigenmodes $\mathbf{u}_g$ and $\mathbf{u}_u$, is studied as a function of p. Energy distribution in surface-based phononic crystal can be attained from the knowledge of the displacement or velocity and stress fields. The fields are typically calculated via coupled-mode theory or scattering theory in Born approximation. These are perturbative approaches. For instance, in this latter approach the SAW solution for the half-infinite Si slab is taken as the zero-order wave (impinging wave) used to evaluate the scattering matrix (the interaction term being brought in by the grating) together with final states modes (scattered waves). Such an approach loses reliability as the SAW frequency increases. Since the penetration depth of the SAW equals its wavelength λ, higher SAW frequencies imply stronger surface confinement and, ultimately, stronger scattering with the periodic grating. This requires considering higher-order terms in the scattering integral equation in order to achieve a reasonably precise solution. For surface-based phononic crystals working in the hypersonic range ($\lambda \leq 1$ μm) the strong confinement is an issue. The theoretical frame here introduced to define the pseudo-SAW, together with the calculations of the composite system eigenmodes, can be exploited to tackle the problem of energy distribution in the system beyond a perturbative approach and the results can be readily translated in a scattering framework.

The definition given in Eq. 3.3 is here extended to account for the time-averaged normalized energy content in the three regions outlined in Fig. 3.2(a) and in the inset of Fig. 3.7,

$$\alpha_x(\nu) \doteq \frac{\langle E_x(\nu)\rangle}{\langle E_{tot}(\nu)\rangle} \ , \quad x = \{A, B, C\} \ . \tag{3.6}$$

In Fig. 3.7 the energy contents $\alpha_x(\tilde{\nu}_g)$ and $\alpha_x(\tilde{\nu}_u)$ are reported for $x =$

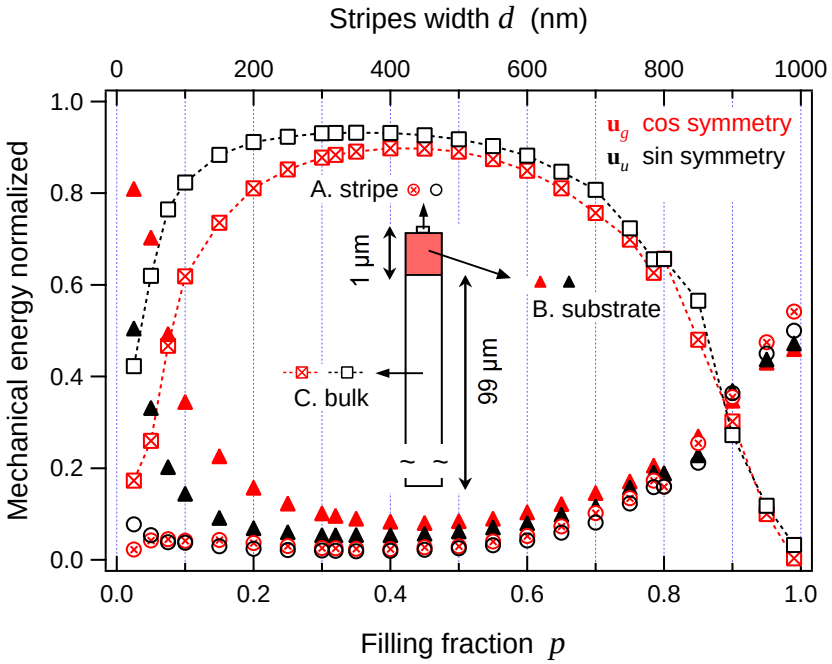

FIGURE 3.7: Analysis of the spatial distribution of the mechanical energy in the composite system over different filling fraction configurations, normalized against the total energy inside the cell. In the inset, the circles represent the fraction of the mechanical energy confined in the nickel stripes region A, the triangles are for the top 1 μm portion B of Si substrate and the squares are associated with the silicon bulk C. The dotted lines are a guide to the eye only.

$\{A, B, C\}$ as a function of the filling fraction p. The results show the mechanical energy spatial distribution (normalized against the total energy inside the cell) over the entire filling fraction range, when a pseudo-SAW eigenmode is excited. For $p = 0$ the SAW is a true eigenmode, the energy being concentrated, as expected for a SAW, in region B: $\alpha_B(\tilde{\nu}) \sim 1$. For small filling fractions ($p < 0.05$), at least for $\mathbf{u}_g$, the elastic energy is mostly concentrated in the 1 μm top portion of the Si slab, where the unperturbed SAW is expected to dump. The grating is much more effective in scattering energy to the bulk for $\mathbf{u}_u$: $\alpha_B(\tilde{\nu}_u) \sim \alpha_C(\tilde{\nu}_u)$. This symmetry-related difference in coupling a SAW to the bulk is a confirmation to the observed relationship $\gamma_u \sim 2\gamma_g$ of Fig. 3.3(a). As p increases to half coverage,

a greater amount of mechanical energy is transferred from the Si surface region B to the bulk region C. From the eigenvalue problem perspective, a greater amount of energy radiated into the bulk translates in energy distributed over a wider range of eigenmodes of decreasing SAW-likeness coefficient $\alpha(\tilde{\nu})$, γ increasing with p for both *gerade* and *ungerade* pseudo-SAWs [see Fig. 3.3(b)]. The maximum values for both $\alpha_C(\tilde{\nu}_g)$ and $\alpha_C(\tilde{\nu}_u)$ are attained for $p = 0.4$, the same filling fraction maximizing $\Delta\tilde{\nu}$. For $p > 0.4$ the trend reverses, being $\partial\alpha_C(\tilde{\nu})/\partial p < 0$ whereas $\partial\alpha_{A,B}(\tilde{\nu})/\partial p > 0$; the relative energy content in the bulk region is transferred in region B and A. For $p \sim 0.8$ the energy content in the Ni stripe equals the energy content in region B; the equality of energy content holds also between sin and cos symmetry eigenmodes and pseudo-SAW frequency crossing occurs (see Fig. 3.5). As the Si full coverage configuration is approached, the radiation into the bulk is further reduced in favor of a strong mechanical energy confinement in the stripe and in the top 1 μm portion of Si substrate, the crossing point being for $p = 0.9$. For $p > 0.9$, the oscillation of the Ni stripe starts to energetically dominate and the stripe behaves as a low-loss acoustic waveguide. The unperturbed SAWs, eigenmodes of the semi-infinite slab, are now heavily scattered into the Ni overlay. In the limit of Si full coverage ($p = 1$), the Ni overlay acts as a lossless waveguide. The SAW is a true solution of the eigenvalue problem, without coupling with bulk modes, and it is downshifted in frequency with respect to the overlay-free SAW by ~ 0.8 GHz.

3.6 Summary

In the present Chapter, we proposed a theoretical frame allowing to access the physics of pseudosurface acoustic waves in surface phononic crystals. The pursued strategy can be applied to any surface phononic crystal, enabling investigation of pseudo-SAW line shapes, gap opening and mechanical energy scattering beyond

perturbative approaches, thus finding application also in the hypersonic frequency range.

We applied the outlined theoretical framework to the case of a hypersonic surface phononic crystal made of periodic nickel stripe on a silicon substrate. We then investigated the pseudosurface acoustic wave frequency gap over the entire filling fraction range, starting from the case where the periodic nanostructures act as a perturbation, to finally reach the substrate full coverage. A preliminary understanding of how the construction parameters affect the frequency gap has been achieved. We showed that the pseudo-SAW frequency gap results from a combination of geometry $\{p, h\}$ and mass loading $\{m, \rho\}$ factors, the two affecting the pseudo-SAW frequencies in opposite ways. A trade-off between p and m is thus necessary for tailoring the pseudo-SAW frequencies or frequency gap for the application at hand. The mechanical energy spatial distribution of pseudo-SAW as a function of the filling fraction has been studied, potentially allowing to tailor the device's parameters in order to minimize the energy content scattered out of the desired modes.

Chapter 4

Calorimetry at the nanoscale

Over the last century, calorimetry has been the method of choice for the investigation on thermodynamic properties of matter. Conventional calorimetry, however, is limited to sample sizes of few tens of micrograms. An alternative route, to overcome the downsizing limits of conventional calorimetry, relies on all-optical time-resolved techniques. In the present Chapter the thermal dynamics occurring in such experiments are theoretically investigated from 300 to 1.5 K. We report ab-initio calculations describing the temperature dependence of the electron-phonon interactions for Cu nanodisks supported on Si. The electrons and phonons temperatures are found to decouple on the ns time scale at ~ 10 K, which is two orders of magnitude in excess with respect to that found for standard low-temperature transport experiments. By accounting for the physics behind our results we suggest an alternative route for overhauling the present knowledge of the electron-phonon decoupling mechanisms in nanoscale systems by replacing the mK temperature requirements of conventional experiments with experiments in the time-domain.

4.1 Introduction

In the last decade the advent of nanoprocessing techniques has emphasized the need for designing non-invasive methodologies to access the realm of the thermal properties of nanoscale systems [75, 76]. As samples dimensions shrink a variety of new phenomena have been observed, such as the quantum of thermal conductance [77], and new refrigeration devices proposed [78]. From an applicative standpoint, issues related to thermal management at the mesoscale constitutes a major technological challenge and are of paramount importance for the electronic industry.

Over the last century calorimetry has been the method of choice for the investigation on thermodynamic properties of matter. Conventional calorimetry, however, is limited to sample sizes of few tens of micrograms. A successful improvement recently arose from micromembrane-based nanocalorimeters [77, 79]. Such devices perform extremely well in terms of sensitivity but their application range is limited to cryogenic temperatures, they lack time-resolution capabilities and samples need on-chip integration.

An alternative route relies on all-optical time-resolved techniques. When tackling the problem of measuring the specific heat of a small object a fast non-contact probe is the optimal choice. The speed requirement is dictated by the fact that the heat exchange between the sample and the thermal reservoir is proportional to the sample's mass. A contact probe of dimensions comparable to the sample's one affects the measurement in that one would access the specific heat of the nanosample and the probe itself. The idea underlying all-optical time-resolved nanocalorimetry is as follows. A thin metal film or metallic nanosample to be investigated is placed in thermal contact with a substrate serving as a thermal bath. An ultrafast laser pump beam serves as the power source, delivering an energy density dU_V to the nanosample. The sample's temperature time relaxation to the substrate is measured via a time-delayed probe beam. Several detection schemes

can be exploited or envisioned. Among them, the time-resolved Near-Infra Red Diffraction (TR-NIRD) technique [1, 80] detects the changes in the diffracted signal modulated by the ordered nanostructures thermal expansion.

4.2 Time-resolved nanocalorimetry

Calorimetry is the method of choice for studying the heat transfer process inside a system. By adopting a Time Relaxation technique, the heat flux is determined from the temperature time evolution, the overall system consisting in a sample in contact with a thermal bath. The aim of an archetypal time-resolved calorimetry experiment is thus to measure the thermalization time of the sample, to the thermal bath, after being warmed up by an external heat source. The thermalization dynamics is described by means of a Time Relaxation model in which it is assumed that the sample is warmed up by an external heat source until time t_0. As shown in Fig. 4.1, the sample reaches the temperature T_0 while the thermal bath temperature T_{sub} remains unchanged. The thermal contact between sample and substrate is described by a thermal resistance R_{th} and parallel channels of energy dissipation are assumed negligible. Under these hypotheses, the temperature evolution in time follows an exponential decay governed by a relaxation time τ:

$$\Delta T(t) = T(t) - T_{sub} = (\Delta T)_0 \, e^{-t/\tau} \ , \tag{4.1}$$

where

$$\tau = C R_{th} \ , \tag{4.2}$$

being $T(t)$ the sample temperature, T_{sub} the fixed thermal bath temperature, R_{th} the thermal resistance, $C = m \cdot C_m$ the sample's thermal capacity, with m the sample's mass and C_m the specific heat per unit of mass. The thermal resistance is directly related to the interface thermal resistivity ρ_{th} trough the equation:

$$R_{th} = \frac{\rho_{th}}{A} \ ; \tag{4.3}$$

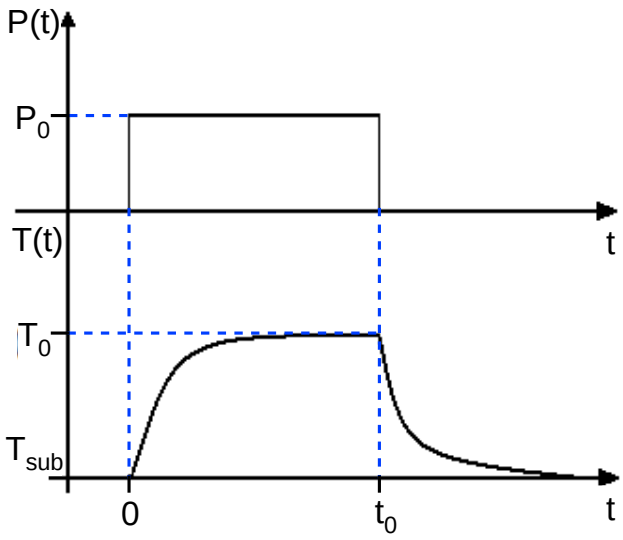

FIGURE 4.1: Thermalization dynamics described by the Time Relaxation Model.

ρ_{th} is a macroscopic quantity accounting for phonons dispersion mismatch on the two sides of the interface and other eventual microscopic mechanisms limiting the heat flow between the sample and the substrate, and A is the sample-thermal bath contact area.

Two fundamental aspects of calorimetry measurements must be considered. First, the thermalization time τ is proportional to the mass: thermal equilibrium is achieved on a shorter time span by samples with lower mass. Typically, as displayed in Fig. 4.2, samples with $m \geq 50$ μg have a relaxation time τ ranging from ms to hundreds of seconds, depending on the material and the characteristics of the thermal contact between sample and heat reservoir. Samples with mass on the order of $10^{-13} - 10^{-15}$ g have $\tau \sim$ ns. The second aspect refers to standard techniques of temperature probing, that adopt thermocouples measuring a voltage drop proportional to the temperature variation [see Fig. 4.3]. The thermocouple probing mechanism does not perturb significantly the system, as far as its mass is much lower compared to the sample's. But as the system dimensions shrink to the nanoscale, such standard calorimetry technique results hard exploitable because

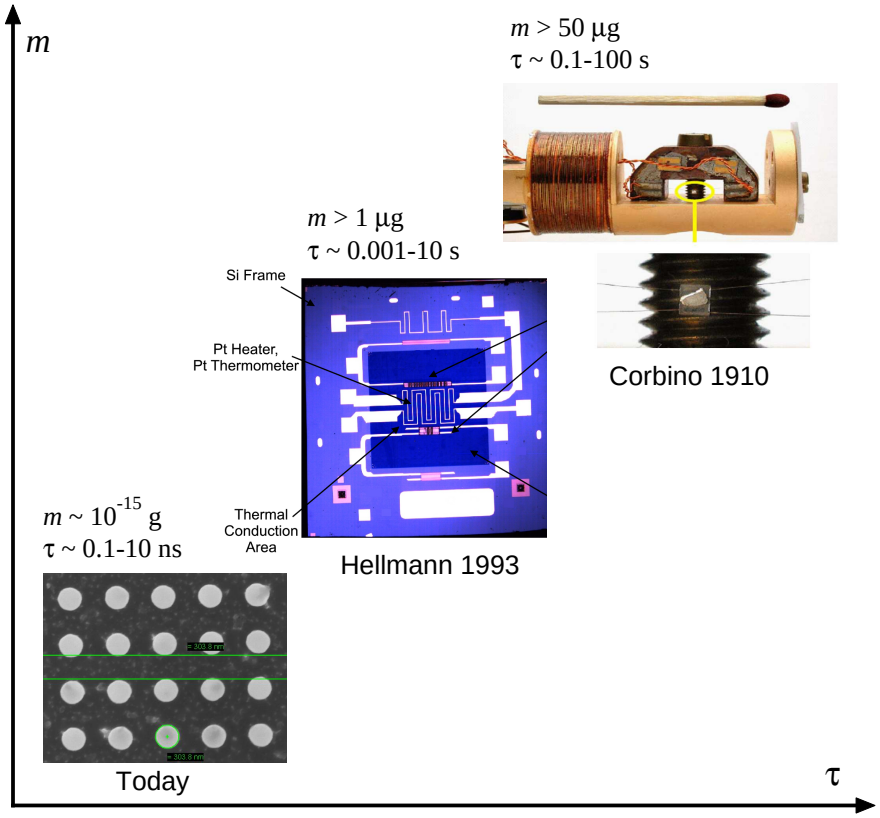

FIGURE 4.2: Examples of the thermalization time τ vs. sample mass m proportionality.

when the sample mass is easy comparable to the mass of the measurement apparatus, the thermal capacitance will have similar contributions from the sample and the thermocouple itself, influencing the system's relaxation time and forbidding the measurement of the sample's specific heat.

All-optical time-resolved calorimetry at the nanoscale is a good candidate to perform calorimetry on mesoscale and nanoscale samples, providing both adequate measuring speed and non-contact probe. For the aim of this Chapter, the sample geometry consists of an array of Cu nanodisks deposited on a Si substrate, the unit cell dimensions are reported in Fig. 4.4. The nanodisks have mass of the order of 10^{-15} g. The bottom of the Si substrate is kept at constant temperature T_{sub} by a cryostat, whereas insulating boundary conditions apply to the Si cell lateral

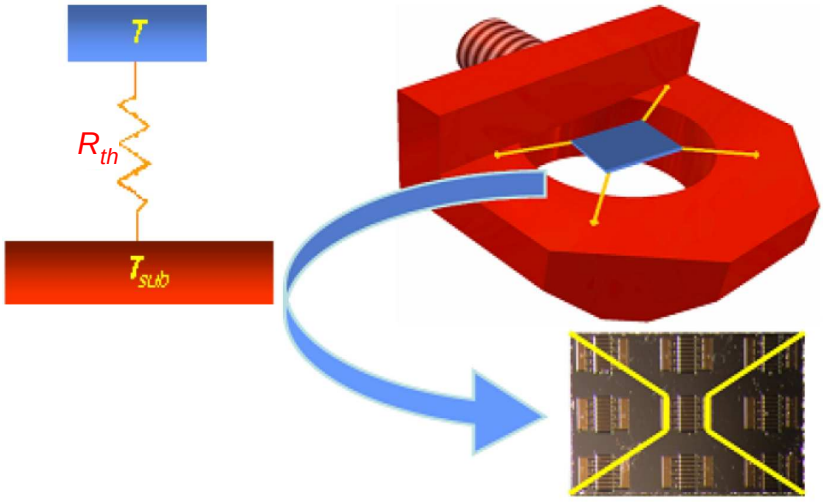

FIGURE 4.3: Standard calorimetry technique (from Ref. [81]): (Left) Scheme of the thermal contact between the sample (blue) and the thermal bath (red) by means of a thermal resistance R_{th}. (Right) Sample holder for standard calorimetry measurements. The thermal contacts are evidenced in yellow.

boundaries.

In a time-resolved framework, after excitation by a single Ti:sapphire pump pulse (120 fs duration, 1 nJ per pulse, wavelength 800 nm, spatial extension 40 μm at FWHM and 1 MHz repetition rate), the thermal evolution problem investigated by the probe pulse is conveniently schematized, at least at ambient temperature, in three steps. In the first step, the laser pump pulse heats the electron gas of the metallic nanodisks (sub-picosecond time scale). In the second step, the hot electron gas thermalizes with the phonons within the disks (picosecond time scale). Finally in the third step, the disk transfers heat δQ_V to the silicon substrate thermalizing with it (nanosecond time scale). After the pump pulse absorption, the nanodisks thermally expand in function of the change in temperature and the metallic disk radius variation is directly followed in the time-resolved probe reflected (or diffracted) signal R:

$$\frac{\Delta R}{R} \propto \frac{\delta a}{a} = \alpha \Delta T \, , \tag{4.4}$$

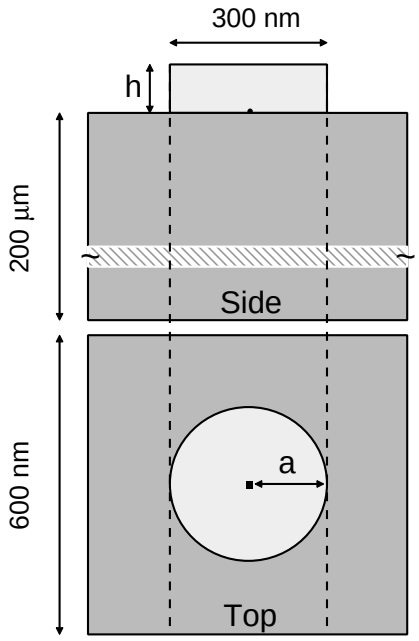

FIGURE 4.4: Side and Top views of the simulation unit cell geometry: $h = 30$ nm.

where a is the nanodisk radius, ΔT is the temperature variation induced by the pump pulse absorption and $\alpha = 16.5 \cdot 10^{-6}$ K^{-1} is the Cu linear thermal expansion coefficient at 297 K. In the present case, the disk radius relative variation is $6.6 \cdot 10^{-5}$, corresponding to an absolute variation of 10^{-10} m. Among the advantages of the time-resolved all-optical technique are the ability to measure relative variations of the Cu nanodisks radius that can range up to 10^{-8}, following α's dependence on temperature ($5 \cdot 10^{-9}$ K^{-1} at 4.2 K), and the possibility to take advantage of time resolution to access the nanostructures thermodynamics in a time domain ranging from fs to ns ($\tau \sim 1$ ns).

4.3 Simple analytic approach

An analytical description of the thermal problem is developed to evaluate the temperature evolution in time and to access the relevant parameters taking place

during the third step of the thermal process [see Section 4.2 for thermal steps labeling]. The initial temperature of the system is assumed to be $T_{sub} = 297$ K and the specific heat of the system, together with the thermal conductivity and interface resistance are considered, for the time being and unless otherwise stated, temperature independent. Further considerations are thus valid at T_{sub} only, but they give anyway an indication of the dynamics induced by a laser pulse on a nanosystem.

The 800 nm laser pulse penetration depth in copper is $\Lambda_{Cu} = 13$ nm and the reflectance at normal incidence is $R_{Cu} = 0.93$; both are derived from copper's optical constants at 297 K ($n_1 = 0.454$, $n_2 = 4.978$, from Ref. [82]). Thus, the energy transmitted in the Cu nanodisk is absorbed in half its volume and, due to its high thermal conductivity $k_{Cu} = 381$ W/mK [83], the disk is isothermal after ~ 2 ps. On the other hand, the laser penetration depth in silicon is 8 μm and, considering Si optical constants and specific heat, the substrate's temperature increase after the pump pulse absorption is negligible compared to the nanostructures. Under these conditions, the thermal problem can be simply described beginning from a metallic disk at a uniform initial temperature T_0 in contact with a Si thermal bath at constant temperature T_{sub}. For simplicity, the problem is solved for a Cu film ($h = 30$ nm) deposited on a Si substrate, reducing the thermal evolution to a 1D calculation in the spatial coordinate z and temporal t, as reported in Fig. 4.5.

A time $t = 0$ the pump pulse raises the film temperature to T_0. Regarding the boundary conditions, the film's top surface ($z = 0$) is thermally insulated while there is a heat flux at $z = h$ regulated by the interface resistivity ρ_{th}. The problem is formulated beginning from the diffusion equation [84]:

$$\frac{\partial^2 T(z,\,t)}{\partial z^2} = \frac{\rho\, C_s}{k}\,\frac{\partial T(z,\,t)}{\partial t} \quad for\ 0 < z < h\ and\ t > 0\ , \tag{4.5}$$

with C_s as the specific heat per unit volume, ρ the film density and k the thermal conductivity.

$$k\frac{\partial T(z,\,t)}{\partial z} = 0 \quad for\ z = 0\ and\ t > 0$$

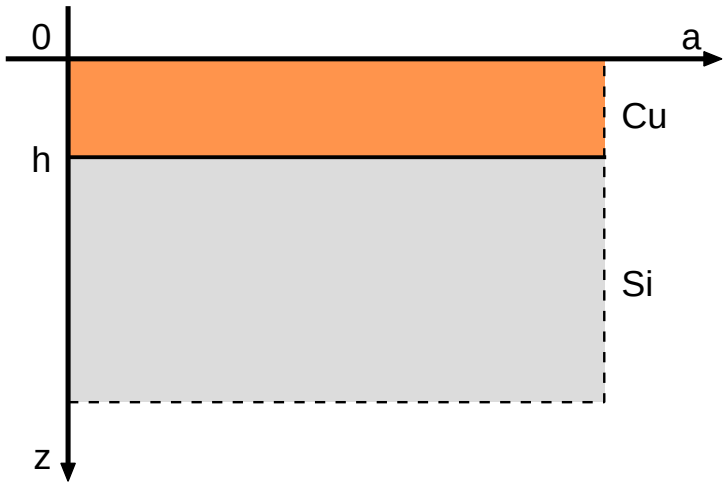

FIGURE 4.5: Geometry of the Cu film deposited on a Si substrate, adopted in the analytical solution of the 1D thermal evolution problem.

$$k\frac{\partial T\left(z,\ t\right)}{\partial z}+\frac{1}{\rho_{th}}\left(T\left(z,\ t\right)-T_{sub}\right)=0\quad for\ z=h\ and\ t>0 \tag{4.6}$$

$$T=T_0\quad for\ 0\leq z\leq h\ and\ t=0$$

The thermodynamics depends on $\Delta T=T-T_{sub}$ and, setting $T_{sub}=0$, the solution to the problem is found separating the variables:

$$T\left(z,\ t\right)=T_0\sum_{m=1}^{\infty}e^{-\frac{\kappa}{h^2}\xi_m^2 t}\frac{2Bi}{\left(\xi_m^2+Bi^2\right)+Bi}\frac{cos\left(\frac{\xi_m}{h}z\right)}{cos\left(\xi_m\right)}\ , \tag{4.7}$$

where $Bi=\frac{h}{k\rho_{th}}$ is the Biot number, $\kappa=\frac{k}{\rho C_s}$ is the thermal diffusivity of the material and ξ_m are roots of the equation:

$$\xi_m tan\left(\xi_m\right)=Bi\ . \tag{4.8}$$

The nanodisk temperature dynamics is readily accessible provided the Biot number $Bi\ll 1$, meaning that the disk remains isothermal during the thermal relaxation process to the substrate. The roots ξ_m depend on Bi, and as seen in Fig. 4.6,

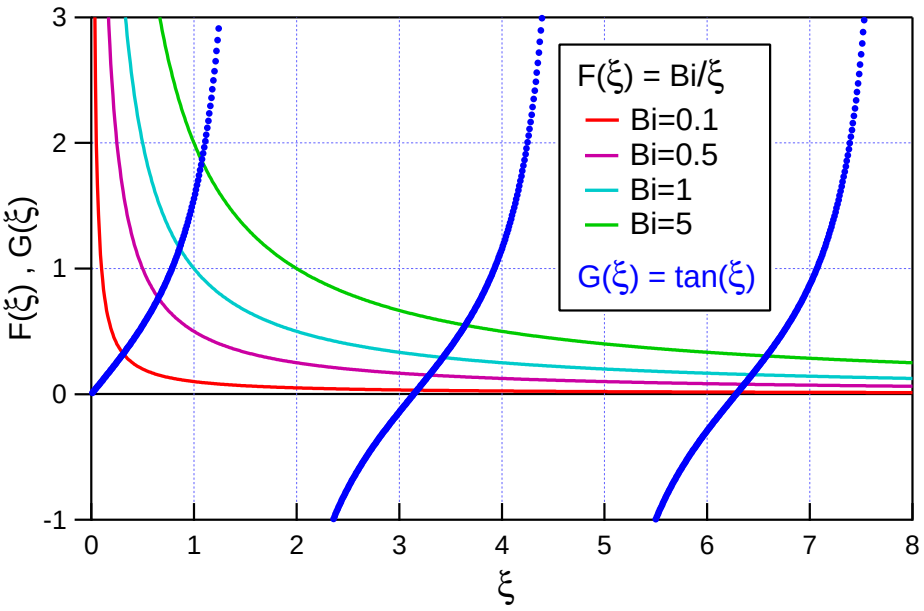

FIGURE 4.6: Graphic solution of Eq. 4.8, for different values of the Biot number.

they are found from the intersection of $G(\xi) = tan(\xi)$ and $F(\xi) = Bi/\xi$, where

$$Bi \to 0 \;\Rightarrow \begin{cases} \xi_1 \to 0 \\ \xi_m \to (m-1)\,\pi \quad m \geq 2 \end{cases} . \tag{4.9}$$

Eq. 4.7 shows the temperature dependence from a series of exponentials, and writing their decaying time as

$$\tau_m = \frac{h^2}{\kappa \xi_m^2} , \tag{4.10}$$

we obtain, for $Bi \to 0$,

$$\frac{\tau_m}{\tau_1} = \frac{\xi_1^2}{\xi_m^2} \to \frac{0}{((m-1)\,\pi)^2} = 0 . \tag{4.11}$$

Under this condition, terms with $m \geq 2$ decay more rapidly with respect to the $m = 1$ term and are negligible, and the temperature space profile from approximates to

$$T(z,\ t) = T_0\, e^{-\frac{\kappa}{h^2}\xi_1^2 t}\, \frac{2Bi}{\left(\xi_1^2 + Bi^2\right) + Bi}\, \frac{cos\left(\frac{\xi_1}{h} z\right)}{cos\,(\xi_1)} , \tag{4.12}$$

with

$$\xi_1 tan\,(\xi_1) \cong \xi_1^2 = Bi . \tag{4.13}$$

Managing Eq. 4.12, we can definitely demonstrate that the condition $Bi \ll 1$ is mandatory to access the thermal relaxation process of the system,

$$\frac{\Delta T}{T} = \frac{T(0,t) - T(h,t)}{T(0,t)} = 1 - cos(\xi_1) \cong 1 - \left(1 - \frac{\xi_1^2}{2} + O\left(\xi_1^4\right)\right) \cong \frac{Bi}{2} \ . \quad (4.14)$$

As shown, $Bi \ll 1$ means a negligible thermal gradient between the top and bottom surfaces of the metallic film (z axis), i.e. the nanostructures remain spatially isothermal throughout the thermal relaxation process to the substrate. On the contrary, a thermal gradient would carry a space dependence of the specific heat, hence the impossibility of defining thermal properties of the nanosample as a whole.

Another point of view can be adopted to clarify the the physical meaning of the Biot number, to this end is useful to compare the thermal conductivity k, as the quantity indicating how effective heat diffusion is within the sample's material, to the interface thermal conductivity $k_{int} = h/\rho_{th}$, a parameter characterizing the effect of the interface and sample's size on the heat transfer process. The Biot number is then cast as:

$$Bi = \frac{k_{int}}{k} \ . \quad (4.15)$$

$Bi \ll 1$ implies that heat conduction inside the sample occurs on a faster time scale when compared to heat dissipation trough the interface with the thermal bath, giving a negligible temperature gradient inside the sample and justifying its state as isothermal during the relaxation process towards the substrate. This calorimetric condition is satisfied for the $h = 30$ nm Cu film on silicon: with $k_{Cu} = 381$ W/mK, $\rho_{th} = 10^{-8}$ m^{2}K/W, the Biot number is $Bi = 7.87 \cdot 10^{-3}$ and estimating the thermal relaxation time we obtain $\tau_1 = \rho C_s h \rho_{th} \sim 1$ ns.

4.4 Full thermodynamical model

The physics entailed in the first two steps of the thermal evolution problem, described in Section 4.2, is well modeled by the Two Temperature Model (2TM) [5]:

$$\begin{aligned} C_{el}(T_{el})\partial_t T_{el} &= P_p(t) - \Gamma(T_{el}, T_{ph}) + \vec{\nabla} \cdot (k_{el}(T_{el})\vec{\nabla} T_{el}) \\ C_{ph}(T_{ph})\partial_t T_{ph} &= \Gamma(T_{el}, T_{ph}) + \vec{\nabla} \cdot (k_{ph}(T_{ph})\vec{\nabla} T_{ph}) \end{aligned} \tag{4.16}$$

k and C indicate the temperature thermal diffusion coefficient and specific heat per unit volume, respectively, while the reference to the electrons (el) or Cu phonons (ph) is indicated by the subscript. Γ is the electron-phonon coupling constant and P_p is the profile of the pulsed power per unit volume absorbed by the sample.

The volumetric energy density absorbed by the sample is peaked within the nanodisk, because of the difference in the optical penetration depth between Cu and Si. This occurrence gives rise to the onset of an heat flux from the nanodisk to the substrate, taking place on the nanosecond time scale (third step). The thermal link translates in the following boundary conditions at the disk-substrate interface:

$$\begin{aligned} \widehat{n}_{ph} \cdot k_{ph}\vec{\nabla} T_{ph} + (T_{ph} - T_{Si})/\rho_{th}(T_{ph}) &= 0 \\ -\widehat{n}_{Si} \cdot k_{Si}\vec{\nabla} T_{pSi} - (T_{ph} - T_{Si})/\rho_{th}(T_{ph}) &= 0 \end{aligned} \tag{4.17}$$

$\widehat{n}_{ph}$ and $\widehat{n}_{Si}$ being the outward unit vector normal to the disk and Si boundary, respectively. As a thermodynamical parameter accounting for microscopic processes such as phonon dispersion mismatch between Cu and Si, the thermal boundary resistivity ρ_{th} actually depends on the temperatures at both sides of the interface via the phonons Bose-Einstein distributions [85, 86]. This dependence is seldom considered, the two temperatures being almost the same, in most applications. In the present work, and on certain time scales, it occurs that T_{ph} exceeds T_{Si} by several tens of degrees Kelvin. For this reason, following the idea underlaying the

formal treatment of the thermal boundary resistivity, the temperature dependence is taken upon the hotter carrier temperature. The temperature within the Si substrate is calculated via the Fourier heat transfer equation.

This three-step sequence repeats itself upon arrival of a new laser pulse, once every 1 μs [87]. The steady-state temperature distribution, due to the pulses train, is modeled following Ref. [1]. This distribution serves as the initial boundary condition for the thermal dynamics following the arrival of a single pulse and is rather constant within the first few microns region beneath the Si-nanodisk interface. In the following the temperature in this region will be addressed as T_{Si}, the temperature calculated in a point positioned 5 nm beneath the disk-Si interface [see Fig. 4.4]. The temperature-dependent specific heats and thermal conductivities entering the equations have been taken from data available in the literature [88].

A fundamental issue is the temperature dependence of the electron-phonon coupling which, in the high temperature limit, reads $\Gamma = G(T_{el} - T_{ph})$. This approximation fails when the thermal dynamics spans the entire temperature range from hundreds of degrees K to liquid Helium temperature. For instance, with T_{sub} set at 4.2 K, T_{el} rises to ~ 100 K within the pump pulse time width, relaxing back to ~ 4.2 K on the ns time scale. In order to properly account for the temperature dependence over such a wide temperature range, the electron-phonon coupling is cast as $\Gamma = [I(T_{el}) - I(T_{ph})]/V$ where

$$I(T) = 2\pi N_c N_{E_F} \int_0^\infty d\omega \alpha^2 F(\omega)(\hbar\omega)^2 n_{BE}(\omega, T) \, , \tag{4.18}$$

with N_c the number of cells in the sample, N_{E_F} the electronic DOS at the Fermi level, n_{BE} the Bose-Einstein distribution and $\alpha^2 F$ the Eliashberg function [89], here calculated ab-initio within the frame of Density-Functional Theory [90]. Simulations results are reliable down to 0.6 THz, the electron-phonon interaction calculation failing for longer phonon wavelengths. For lower frequencies $\alpha^2 F = \tilde{\lambda}\omega^2/\omega_D^2$ [89, 91], ω_D being the Debye frequency and $\tilde{\lambda}$ a fitting parameter. The value $\tilde{\lambda}$ has been set as to have $I(T)$ matching the experimental data

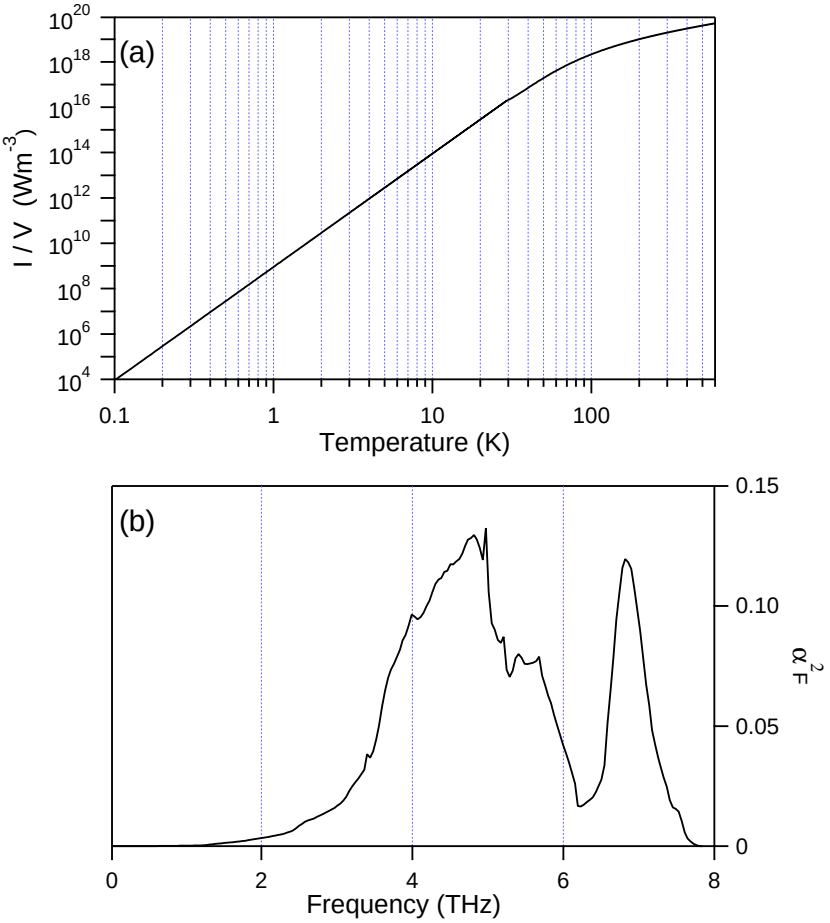

FIGURE 4.7: (a) Interaction term $I(T)/V$ in log-log scale obtained from numerical integration of Eq. 4.18. (b) Eliashberg function $\alpha^2 F$ obtained from ab-initio Density Functional-based calculations.

reported at sub-K temperatures [78]. The coefficient G occurring in the expression for the high temperature electron-phonon interaction, obtained from the linear fit of $I(T)/V$ for $T \geq \Theta_D$, with Θ_D the Debye temperature, is $8.43 \cdot 10^{16}$ W/(m^{3}K), in good agreement with experimental values reported in the literature [92, 93]. Results for both $I(T)/V$ and $\alpha^2 F$ are shown respectively in Figs. 4.7(a) and 4.7(b). Attention is drawn on the nine orders of magnitude change of the interaction term in the temperature range of interest for this work, i.e. from ambient temperature to 1.5 K.

The thermal boundary resistivity is well modeled by the Acoustic Mismatch Model (AMM): $\rho_{th}(T) = A_{bd}T^{-3}$ for $T \leq \widetilde{T} = 30$ K with $A_{bd} = 1.4{\cdot}10^{-3}$ K^{4}m^{2}W^{-1} specific for a Cu-Si interface [94]. For higher temperatures, ρ_{th} is taken at the constant value $A_{bd}\widetilde{T}^{-3}$, that is within the range of values reported for ambient temperature. Nevertheless, to dissipate all doubts regarding the dependence of our findings on the detailed value of $\widetilde{T}$, calculations have been performed with values of $\widetilde{T}$ spanning the range 20-50 K without affecting the physics.

4.5 Results and discussion

The focus of the present Chapter is on the relaxation dynamics relevant for nanocalorimetry, therefore only the time scale from 100 ps to 10 ns will be discussed. Simulations results at ambient and liquid Nitrogen temperatures are reported in Fig. 4.8. In both cases the temperature within the nanodisk is well defined (T_{el}=T_{ph}) and remains homogeneous throughout its volume, thus assuring thermodynamical equilibrium between electrons and phonons and the technique's applicability to investigate the nanodisk thermal dynamics.

At T_{sub}=297.5 K the Si substrate acts as a thermal reservoir at constant temperature, while the disk temperature time dependence is fitted by a single decaying exponential with time constant $\tau_1 = 1.1$ ns [Fig. 4.8(a)]. The maximum relative change of the nanodisk specific heat, $\Delta C_{ph}/C_{ph}$=$1.14{\cdot}10^{-3}$, allows disregarding its temperature dependence. These results suggest modeling the problem as an isothermal film, with initial temperature 301 K, thermally linked with a reservoir at T_{Si}=298 K [see Section 4.3]. A value of the Biot number $Bi = h/k_{ph}\rho_{th} \sim 10^{-3}$ guarantees the disk remains isothermal throughout the thermal relaxation process. Under these circumstances the analytic solution for the disk temperature follows a single exponential decay [84], with time constant $\tau = 1$ ns, in agreement with the fit to the numerical simulation, and the nanodisk specific heat is readily accessible

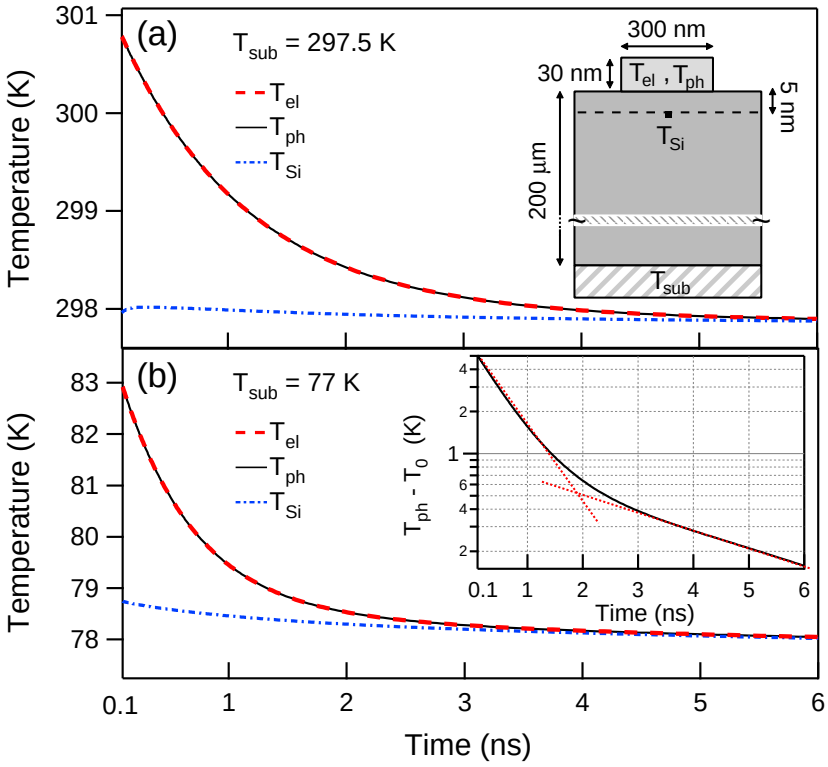

FIGURE 4.8: Thermal relaxation dynamics results of the simulations for (a) $T_{sub} = 297.5$ K and (b) $T_{sub} = 77$ K. Insets: (a) Locations within the sample were the temperatures are calculated. (b) Difference between T_{ph} and its asymptotic value T_0, in semi-log scale. Dashed red lines are a guide to the eye, showing double exponential behavior.

as $\tau/h\rho_{th}$.

At $T_{sub} = 77$ K, the nanodisk temperature dynamics is well fitted by a double exponential with decay times $\tau_1 = 0.617$ ns and $\tau_2 = 6.286$ ns, respectively [Fig. 4.8(b)]. On the contrary to the previous case, T_{Si} is not constant, due to the diminishing of C_{Si} with temperature. The physics can be rationalized as follows: the isothermal nanodisk "feels" a substrate constant temperature on the sub-ps time scale and it thermalizes with it with $\tau = 0.622$ ns, as calculated on the basis of the isothermal disk model adopted above. This interpretation is supported by the agreement between the model-calculated τ and the value τ_1 from numerical

simulations . On the longer time scale the disk and the Si substrate portion in close proximity to the disk-Si interface jointly thermalize with the rest of the Si substrate.

The physics changes drastically for T_{sub} in the range of liquid He temperatures. Simulations results for $T_{sub} = 1.5$ K are reported in Fig. 4.9. T_{el} and T_{ph} decouple at 13 K, 1 ns after the pump pulse arrival, with a maximum relative temperature variation of 22%, for a time delay of 2.2 ns. A similar result, with relative temperature variation of 6%, is found for $T_{sub} = 4.2$ K. From transport measurements in mesoscopic structures the electron-phonon temperature decoupling occurs at sub-K temperatures [78, 95], whereas for the present system our model foresees the decoupling at temperatures about two orders of magnitude higher. Interestingly here is to point out that the electron-phonon decoupling predicted in the present work, cannot be observed by transport measurements because of the lack of time resolution, thus rising a strong demand for ultrafast time-resolved nanocalorimetry.

The physics entailed in the calculations is conveniently unfolded as follows. The substrate temperature beneath the nanodisk reaches its asymptotic value of 2.2 K for a time delay of 1 ns. The system thermal dynamics is then well described in a Two Dimensional (2D) phase space of coordinates (T_{ph}, T_{el}) by the following set of equations,

$$\begin{aligned} \partial_t T_{el} &= -\Gamma(T_{el}, T_{ph})/C_{el}(T_{el}) \\ \partial_t T_{ph} &= -\Omega(T_{ph})/C_{ph}(T_{ph}) + \Gamma(T_{el}, T_{ph})/C_{ph}(T_{ph}) \end{aligned} \tag{4.19}$$

where the thermal flux per unit volume to the Si slab is taken into account by $\Omega(T_{ph})=(T_{ph} - 2.2K)/h\rho_{th}(T_{ph})$. The thermal conductivities within the disk have been omitted, the simulation results showing that the temperature distribution within the disk is spatially uniform over the ns time scale, for both electrons and phonons temperatures. Eq. 4.19 represent the velocity component in the 2D

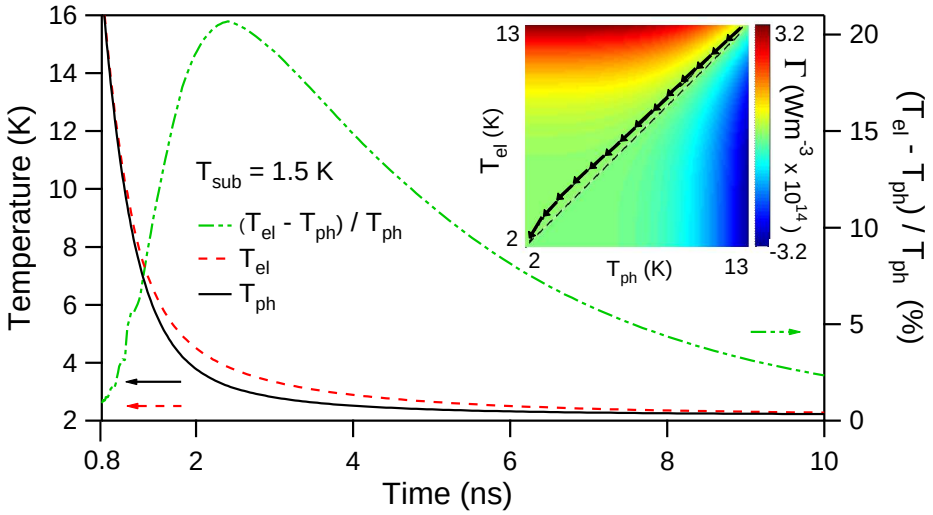

FIGURE 4.9: Thermal relaxation dynamics results of the simulation for T_{sub} = 1.5 K. Left axis: T_{ph} and T_{el}. Right axis: relative temperature variation in percentage. Inset: nanodisk trajectory in phase space for $T < 13$ K (arrows) and T_{el}=T_{ph} reference line (dashed) superimposed on the interaction landscape Γ.

phase space, the initial conditions being the temperatures (T_{ph}, T_{el}) reached for a 1 ns delay. The nanodisk trajectory in phase space is tangent to the velocity field, $(\partial_t T_{ph}, \partial_t T_{el})$. The trajectory is the line $T_{ph} = T_{el}$ for time delays spanning the ps to 1 ns range, the velocity vector pointing along this direction. At 13 K, $\partial_t T_{ph} > \partial_t T_{el}$ and the trajectory changes accordingly, hence $T_{ph} < T_{el}$. The velocity field is ruled by the interplay among Ω, the specific heats and Γ. The Γ interaction term is large enough in the whereabouts of $T_{ph} = T_{el}$ to keep T_{ph} and T_{el} anchored down to 13 K, not so between 13 K and 2.2 K. The trajectory in phase space for $T < 13$ K is reported, superposed on the landscape Γ, in the inset of Fig. 4.9.

When compared with the results obtained for Cu nanodisks, the values for Ω, Γ and the specific heats for several metals in the temperature range were the decoupling is here shown to take place, suggest the present finding should occur in a wider range of materials other than Cu. To this aim an approximate analytic approach is here proposed, also serving as a valuable tool to further highlight

the physical quantities ruling the electron-phonon temperature decoupling. In the low temperature limit, $T \ll \Theta_D$, well satisfied in the temperature range were the decoupling occurs, the interaction term approximates to $I(T) = (\Sigma_0/V)\, T^5$, Σ_0/V being the sub-K electron-phonon coupling constant [78]. The Debye model for C_{ph} applies, and Eq. 4.19 reads

$$\partial_t T_{el} = -C_1 \left(\frac{\Sigma_0}{V}\right) \frac{1}{N_{E_F}} \left(\frac{T_{el}^5 - T_{ph}^5}{T_{el}}\right) \tag{4.20}$$

$$\partial_t T_{ph} = -C_2 \frac{\Theta_D^3}{n A_{bd}} \left(T_{ph} - T_{Si}\right) + C_3 \left(\frac{\Sigma_0}{V}\right) \frac{\Theta_D^3}{n} \left(\frac{T_{el}^5 - T_{ph}^5}{T_{ph}^3}\right) \tag{4.21}$$

with C_1, C_2 and C_3 positive material-independent constants, and n the number of ions per unit volume of the chosen metal. In the case of a Cu nanodisk, $\partial_t T_{ph} < 0$ at all times, thus $\partial_t T_{ph}$ is ruled by the power density delivered from the nanodisk's phonons to the substrate rather than the power density input from the electron to the phonon gas, hence the first term of the sum in Eq. 4.21 dominates over the second term.

Let's now consider Al nanodisks instead and compare it to the Cu nanodisks case. With reference to Eq. 4.21, the following ratios are calculated,

$$\left(\partial_t T_{el}\right)_{Al} / \left(\partial_t T_{el}\right)_{Cu} \sim 0.05$$

$$\left(\frac{\Theta_D^3}{n A_{bd}}\right)_{Al} / \left(\frac{\Theta_D^3}{n A_{bd}}\right)_{Cu} \sim 2.37$$

$$\left(\frac{\Sigma_0}{V}\frac{\Theta_D^3}{n}\right)_{Al} / \left(\frac{\Sigma_0}{V}\frac{\Theta_D^3}{n}\right)_{Cu} \sim 0.2$$

The first ratio signifies that T_{el} remains rather constant in the Al nanodisk as compared to the Cu case, whereas the last two ratios imply that the main contribution to $\partial_t T_{ph}$, also for the Al case, is the power density flow from the phonon gas to the Si substrate and that T_{ph} relaxes to the substrate temperature two times faster than in the case of Cu nanodisks. The electron-phonon temperature decoupling is therefore expected to be more drastic in Al nanodisks as compared to the Cu

case, the main role being played by Θ_D and the material-dependent constants entering Σ_0.

4.6 Summary

In conclusion, by modeling ab-initio the thermal dynamics induced by ultrashort laser pulses in nanoscale systems we show that the break-down of thermodynamical equilibrium between electrons and phonons on the ns time scale takes place at ~ 10 K. This temperature is two order of magnitudes higher than that observed in standard transport measurements. These findings set the limits of applicability of ultrafast nanocalorimetry well above liquid He temperature, the electron-phonon temperature decoupling preventing a proper definition of the temperature concept of the nanosample as a whole. Finally, the present work, while making available a proper tool for interpreting all-optical time-resolved nanocalorimetry experiments, suggests a new route for investigating the physics of the electron-phonon decoupling where the sub-Kelvin temperature requirement is substituted by the ns time resolution. If confirmed by the experiments, this discovery will bridge the fields of ultrafast optics and cryogenic transport in mesoscopic systems, while setting the investigation of the thermodynamics at the nanoscale into a new perspective.

Chapter 5

Thermomechanics of hypersonic surface phononic crystals

We present a theoretical framework allowing to properly investigate the ultrafast optical generation of pseudosurface acoustic waves in a hypersonic surface phononic crystal. Exploiting finite-elements analysis and putting at work the models developed in the previous Chapters, we follow step by step in the time domain the initial impulsive heat-driven displacement launching pseudo-SAWs and evaluate their lifetime. Our calculations are tested against time-resolved optical diffraction measurements performed on the same composite systems [1].

5.1 Introduction

The use of ultrafast laser pulses (pulse duration $\leq$ 1 ps) to generate and detect thermomechanical transients in matter opened the field of picoseconds ultrasonics [2]. In recent years, following the technological progress of transducers and sources of coherent acoustic excitations in the gigahertz range, time-resolved reflectivity experiments performed on gratings of metallic nanometric stripes (2D confined) on transparent (SiO_2) or semitransparent (Si) substrates, evidenced oscillations in the hypersonic range [23, 40, 63, 74], triggering extensive studies on the thermomechanical properties of solid state mesoscale systems.

As described in Chapter 3, the full mechanical problem has been addressed beyond the simple perturbative approach, and pseudo-SAW solutions have been identified and calculated. In a realistic physical scenario, there is no distinction between the eigenmodes of nanostructures and SAWs, the solution of the elastic equation being a pseudo-SAW partially localized on the nanostructures and radiating energy into the bulk [45].

To gain further understanding of the detailed mechanisms behind the optical generation of pseudosurface acoustic waves in hypersonic surface phononic crystals, in this Chapter we combine the mechanical model addressed in Chapter 3 with the thermal expansion model introduced in Chapter 4 to follow step by step in the time domain the initial impulsive heat-driven displacement launching pseudo-SAWs and to evaluate their lifetime. For simplicity, the simulations are first performed in a two-dimensional (2D) geometry, reproducing a surface phononic crystals made of periodic stripes. The thermomechanical time-dependent model is then extended to the three-dimensional (3D) case, with the aim of reproducing the physics of a metallic nanodisks on silicon phononic crystal geometry excited by a laser pulse, and to benchmark our results against those from time-resolved infrared diffraction experiments performed by Giannetti et al. on similar composite systems [1]. The results give credence to our theoretical framework as a unique tool to understand

the detailed thermomechanics of hypersonic surface phononic crystals.

This Chapter is organized as follows: in Section 5.2 we introduce the time-dependent numerical model for time-resolved diffraction measurements. Section 5.3 focuses on the first two steps of the thermomechanical evolution problem, dealing with the impulsive heat-driven displacement. In Section 5.4 we aim at quantitative evaluation of the pseudo-SAW coupling to bulk modes and the lifetime of surface oscillations, further accurately testing the soundness of this thermomechanical time-dependent model on its extension to the three-dimensional (3D) case in Section 5.5.

5.2 Time-dependent model for time-resolved diffraction measurements

In this framework, the surface phononic crystal under investigation has the same characteristics of that in Section 3.2. It is an elastic continuum composed of a periodic metallic grating deposited on a silicon substrate, as reported in Fig. 3.1. We consider the general 2D geometry configuration where elastic isotropic nickel stripes of chosen width $d = 320$ nm and height $h = 50$ nm are deposited on a crystalline silicon substrate. The grating has period $\lambda = 1$ μm, ensuring pseudo-SAWs in the hypersonic range. The time-dependent acoustic equation of motion governing the displacement $\mathbf{u}(\mathbf{r}, t)$ of the composite system is

$$\partial_j \left[c_{ijmn}\left(\mathbf{r}\right) \partial_n u_m \right] = \rho\left(\mathbf{r}\right) \ddot{u}_i \ , \tag{5.1}$$

where $\rho\left(\mathbf{r}\right)$ and $c_{ijmn}\left(\mathbf{r}\right)$ are the position-dependent mass density and elastic stiffness tensor, respectively, the summation convention over repeated indices being assumed.

Carrying on the investigation in the time domain, we solve the time-dependent problem via a transient finite-elements method [69]. The simulation unit cell is

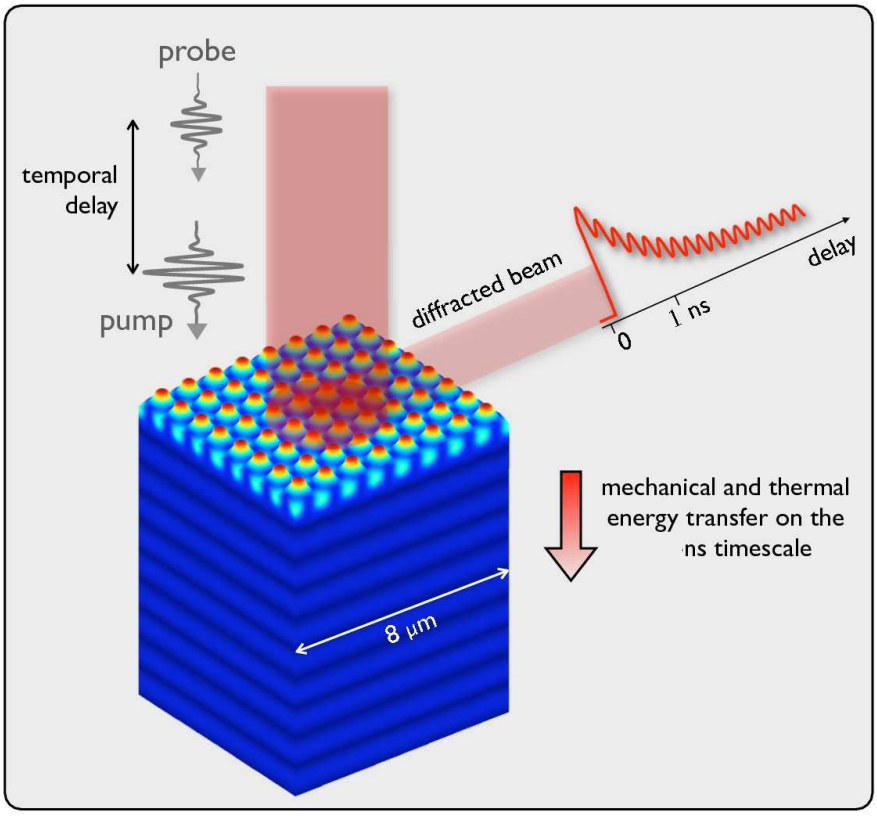

FIGURE 5.1: Schematic diagram of the experimental diffraction technique implemented to generate and detect thermomechanical transients in hypersonic surface phononic crystals.

the one reported in Fig. 3.2(a), the model consisting of a 2D silicon rectangular cell with a nickel stripe on top, and with the same periodic boundary conditions described in Section 3.2. The material properties for the silicon substrate and the nickel stripes, entering the expression of the elastic stiffness tensor, are listed in Table 3.1. A fine quadratic-ordered mesh is chosen for accurate displacements calculations, to account for the size discrepancy between the nanostructure and the silicon cell.

For a clear understanding of the time-dependent acoustic dynamics, a description of the experimental diffraction technique adopted to optically excite and detect pseudosurface acoustic waves in the GHz range is here reported. The basic

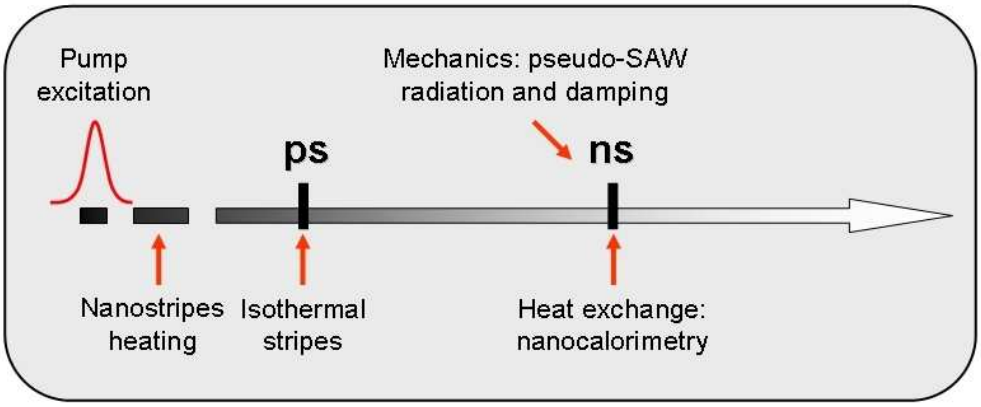

FIGURE 5.2: Schematic diagram of the three timescales spanned by the thermomechanical evolution problem.

idea is to use sub-ps laser pulses in a "percussion" approach (Ti:sapphire oscillator with 120 fs pulse duration, 1 nJ per pulse, 800 nm central wavelength, 55 μm spatial extension at FWHM and 1 MHz repetition rate), in which an intense pump pulse focused on an area A of a solid surface impulsively delivers an energy Q within the light penetration depth Λ, inducing a non-equilibrium local heating of both electrons and lattice on the ps timescale. The local temperature increase ΔT is coupled to a sudden lattice expansion through the thermal expansion coefficient α. The photoinduced thermoelastic stress is able to launch strain pulses $\eta(y,t)$ propagating away from the excited surface along the direction y at the longitudinal sound velocity v. The propagation of strain pulses is followed by means of a second delayed probe pulse. A schematic diagram of the technique is reported in Fig. 5.1, and described in Refs. [1, 80].

The impulsive expansion of the periodic nanostructures mechanically coupled to the substrate, triggers a spatially modulated stress on the silicon surface and launches a pseudo-SAW of wavelength λ matching the nanostripes periodicity. As described in Section 4.3 and presented schematically in Fig. 5.2, after excitation by a single pump pulse, the thermomechanical evolution problem spans three timescales. In the first step, the laser short pulse heats the electron gas of

the metallic stripes (subpicosecond timescale). In the second step, the hot electron gas thermalizes with the lattice (picosecond timescale). In the third step, two occurrences take place: (a) a pseudo-SAW is launched in the system, finally transferring mechanical energy to the Si bulk, and (b) the stripes thermalize with the silicon substrate (sub-nanosecond and nanosecond timescale). This three-steps sequence repeats itself upon arrival of a new laser pulse.

5.3 Impulsive heat-driven displacement

Focusing on the first two steps of the thermomechanical evolution problem, we consider the laser energy density absorbed by the nanostructures and by the substrate, and the specific heat of both Ni and Si. From the simulation of the laser impulsive heating, we are able to follow in time the electron T_{el} and phonon T_{ph} temperatures of the metallic nanostructure, and estimate that within 10 ps the electron gas has effectively thermalized with the lattice and the temperature of the nanostripes is homogeneously increased by ~ 8 K, whereas the substrate temperature T_{Si} is essentially unvaried due to the different penetration depth of the 800 nm radiation, as observed in Section 4.3.

The calculated $T_{el} = T_{ph}$ temperature profile at $t = 10$ ps is reported in Fig. 5.3(a). The impulsive temperature mismatch $\Delta T = T_{ph} - T_{Si} = 8$ K triggers the non-equilibrium expansion of the nanostripes width d, ruled by Eq. 4.4,

$$\frac{\delta d}{d} = \alpha^* \Delta T \sim 2 \cdot 10^{-5} \,, \tag{5.2}$$

α^* being the effective thermal expansion coefficient of the Ni-Si system, with a periodicity given by the stripes' repeat distance. The total displacement profile of the expanded nanostripe at $t = 10$ ps is presented in Fig. 5.3(b).

The analysis of the initial displacement profile, and of the subsequent mechanical time evolution, points out that the initial thermal expansion mainly launches

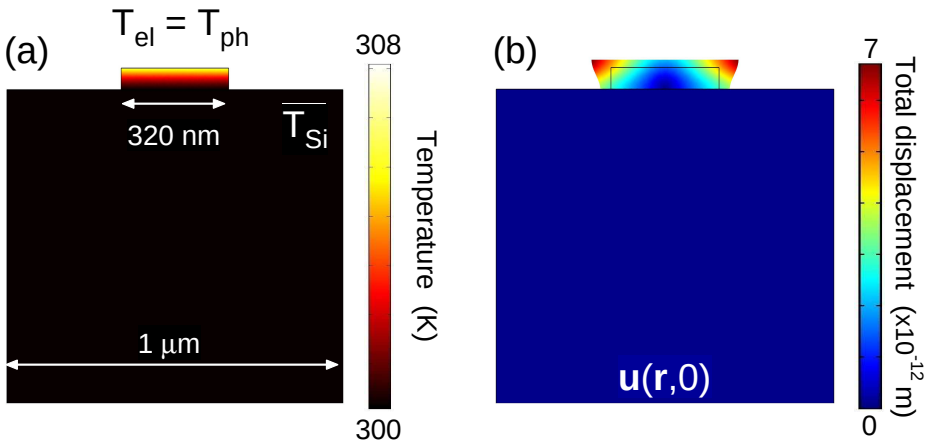

FIGURE 5.3: (a) Calculated $T_{el} = T_{ph}$ temperature profile of the metallic nanostripe at $t = 10$ ps. (b) Total displacement profile of the expanded nanostripe calculated at $t = 10$ ps.

pseudosurface acoustic modes. Reporting on the temporal evolution of the strain pulse launched by the photoinduced thermoelastic stress, we are able to follow step by step the pseudo-SAW dynamics and observe the propagation of the displacement away from the excited surface. As shown in Fig. 5.4, on the sub-nanosecond time scale the spatially modulated stress on the silicon surface launches a pseudo-SAW of wavelength λ matching the nanostripes periodicity. The oscillation is mainly localized on the substrate's top surface, and it has a displacement component evolving into the bulk of the system, verifying the pseudo-SAW definition given in Ref. [45]. Following the dynamics in the pictured sequence, in the first two frames we observe the birth process of the pseudosurface oscillation. In the subsequent frames and more accurately in Fig. 5.5 with a wider landscape observation, we are able to evaluate its localization and we actually distinguish the wavefront of the elastic energy radiation component propagating to the bottom of the silicon cell while the pseudo-SAW, still surface-localized, damps in time.

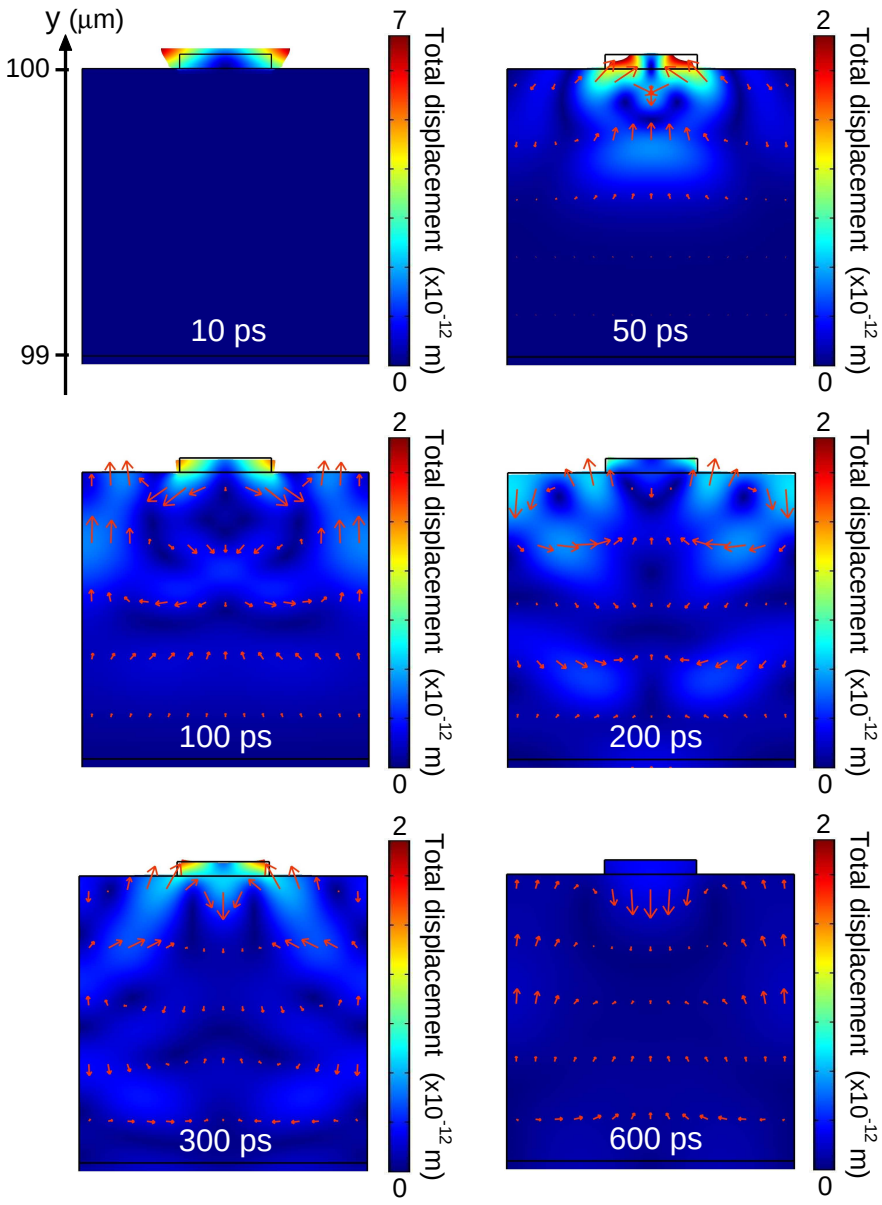

FIGURE 5.4: Close sequence of the pseudo-SAW generation and short range temporal evolution. The profile deformation and arrows correspond to the displacement field. The color scales refer to the absolute total displacement.

5.4 Coupling to bulk modes and lifetime

We now aim at the quantitative evaluation of the pseudo-SAW coupling to bulk modes and the lifetime of surface oscillations. In Chapter 3, we have solved the

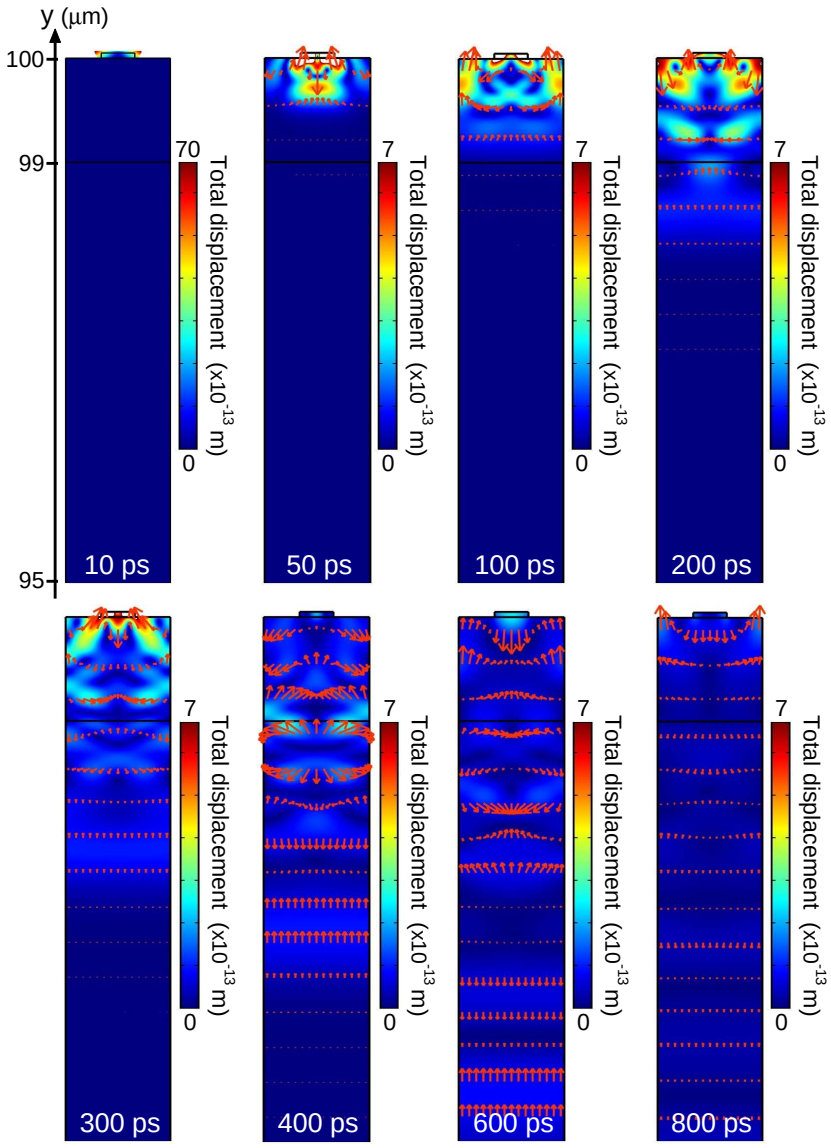

FIGURE 5.5: Landscape view of the pseudo-SAW generation and long range temporal evolution. The profile deformation and arrows correspond to the displacement field. The color scales refer to the absolute total displacement.

acoustic eigenvalue problem [Eq. 3.2]

$$\nabla \cdot (c\nabla \mathbf{u}_i) = -\rho\omega^2 \mathbf{u}_i \ , \tag{5.3}$$

and shown the results of the calculations performed considering the real dimensions of the samples. The analysis of the large number of calculated eigenmodes was

performed exploiting the ratio between the elastic energy content within the 1 μm top portion of the unit cell and within the entire cell, reported as a function of frequency. This quantity, named SAW-likeness coefficient, accounts for the different surface energy content of the calculated eigenmodes [45]. Two Lorentzian curves emerge as the main contribution to pseudo-SAW solutions [see Fig. 3.3]. In particular, the low-energy one is related to sin-like symmetry solutions, whereas the high-energy one has cos-like symmetry, the energy difference between the two modes being the phononic gap opening due to the periodicity of the system. We have shown that the bulk mechanical energy content of the cos-like pseudo-SAW eigenmode properly accounts for the energy radiated into the bulk [see Fig. 3.7].

In this frame, among all the solutions of the acoustic eigenvalue problem, the thermally triggered initial displacement $\mathbf{u}(\mathbf{r}, t = 0)$, significantly overlaps to the superposition of cos-like pseudo-SAW eigenmodes,

$$\mathbf{u}(\mathbf{r}, 0) = \sum_i A_i \mathbf{u}_i(\mathbf{r}) \ , \tag{5.4}$$

with A_i significantly different from zero only for cos-like eigenmodes. As qualitatively observed in Fig. 5.6, the superposition of the displacement of the first two symmetric pseudo-SAWs $\mathbf{u}_{1H}(\mathbf{r})$ (fundamental) and $\mathbf{u}_{2H}(\mathbf{r})$ (second harmonic), solutions of the acoustic eigenvalue problem, well reproduces the initial system expansion $\mathbf{u}(\mathbf{r}, 0)$.

With the aim of evaluating quantitatively the lifetime of the pseudo-SAW coupled to bulk modes, we take inspiration from quantum mechanics writing the general expression of the projection of the time-dependent displacement on the set of acoustic eigenvectors $\{\mathbf{u}_i\}$, solutions of the acoustic eigenvalue problem [Eq. 5.3],

$$|\mathbf{u}(\mathbf{r}, t)\rangle = \sum_i \langle \mathbf{u}_i | \mathbf{u}(\mathbf{r}, t)\rangle \, |\mathbf{u}_i\rangle \ . \tag{5.5}$$

The time-dependent projection coefficient $W_i = \langle \mathbf{u}_i | \mathbf{u}(\mathbf{r}, t)\rangle = c_i e^{i\omega_i t}$ tells us how the displacement at time t is reproduced by the solution $\mathbf{u}_i$ and it is the quantity we employ to spot out which, among the eigenmodes of the composite system, are

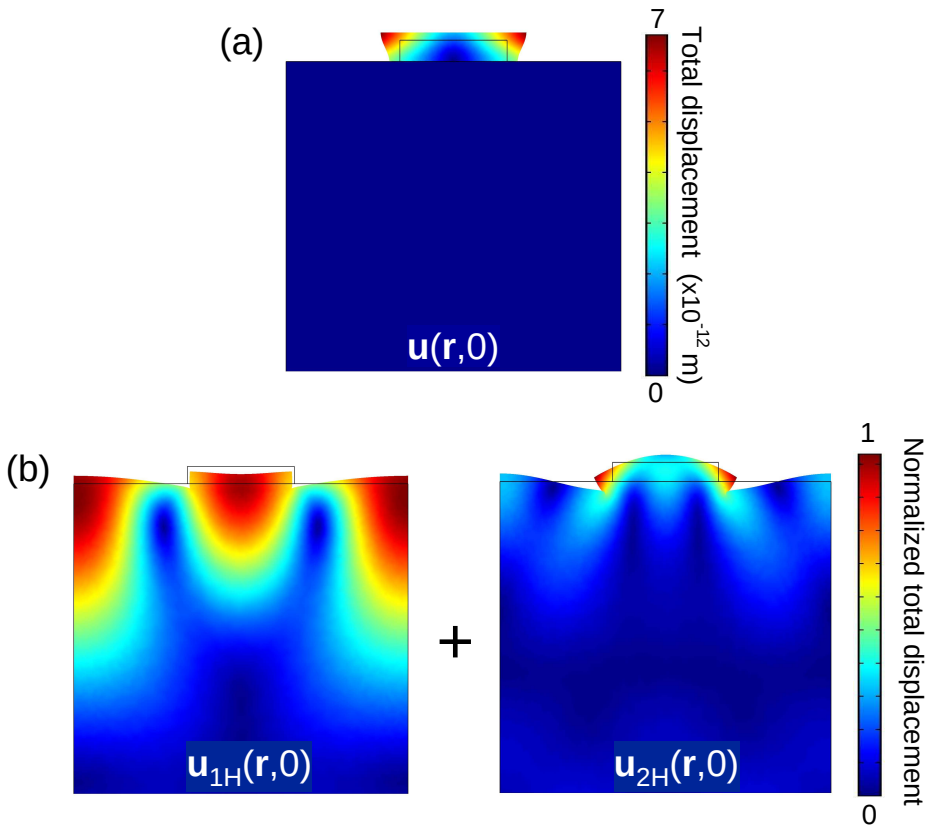

FIGURE 5.6: (a) Total displacement profile of the expanded nanostripe calculated at $t = 10$ ps. (b) Normalized total displacement of the fundamental (Left - $\nu_{1H} = 4.61$ GHz) and second harmonic (Right - $\nu_{2H} = 8.66$ GHz) cos-like pseudo-SAW solutions of the acoustic eigenvalue problem.

mainly excited by the impulsive thermal expansion of the nanostructures at $t = 0$.

In this frame, the evaluation of the projection coefficients requires a normalization of the eigenvalues displacement in terms of the total energy dU absorbed by the nanostructure in the impulsive thermal expansion process. An approximate evaluation follows from the formula $dU = C_V V \Delta T$, that with $\Delta T = 8$ K accounts for the impulsive temperature mismatch triggering the non-equilibrium expansion of the nanostripe, and where $C_V = 2.2 \cdot 10^6$ J/(m^{3}K) is the volume V dependent specific heat. Taking the length of the nanostripe equal to the laser spot diameter, we obtain $dU = 15.5$ pJ/pulse. Writing the expression for dU in terms of

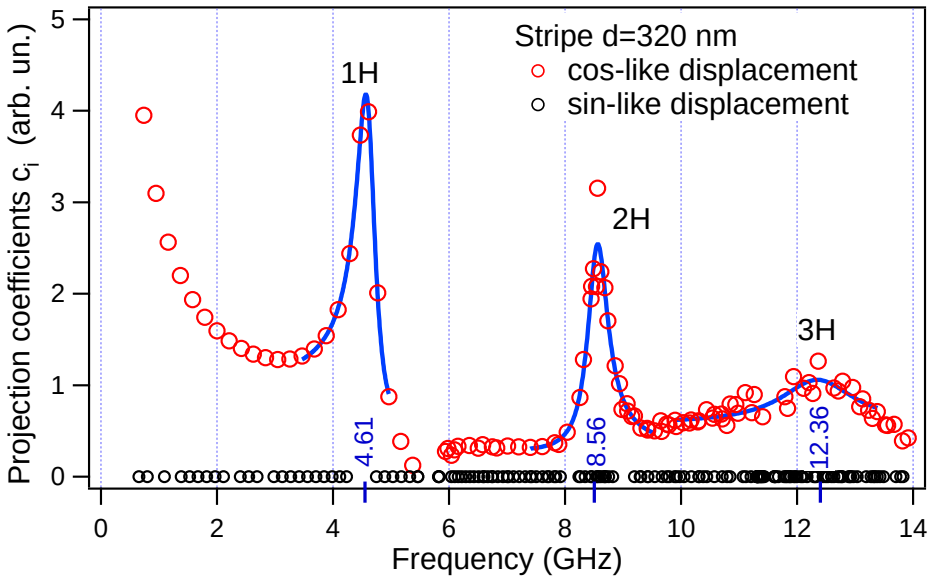

FIGURE 5.7: Projection (2D) of the initial thermal expansion displacement on the eigenmodes of the composite system, with cos-like (red circles) and sin-like (black circles) displacement symmetry. The calculated curves with cos-like displacement symmetry are fitted with the Fano function described in Eq. 5.9 (blue line).

the volume density ρ, the eigenfrequency ω and the displacement $u(\omega)$, as for an harmonic oscillator, we obtain

$$dU = \omega^2 \int_V \rho \left(Au\left(\omega\right)\right)^2 dV \ , \tag{5.6}$$

and we determine the normalized eigenvalue displacement in terms of the normalization coefficient A_i,

$$\tilde{\mathbf{u}}_i = A_i \mathbf{u}_i = \sqrt{\frac{dU}{\omega_i^2 \int_V \rho u^2\left(\omega_i\right) dV}} \mathbf{u}_i \ , \tag{5.7}$$

where the set of eigenvectors $\{\mathbf{u}_i\}$ is normalized to 1. Setting our initial condition of impulsive thermal expansion, we thus rewrite for $t = 0$ the projection expression of Eq. 5.5,

$$\left|\mathbf{u}\left(\mathbf{r},0\right)\right\rangle = \sum_i \langle\tilde{\mathbf{u}}_i|\mathbf{u}\left(\mathbf{r},0\right)\rangle \left|\tilde{\mathbf{u}}_i\right\rangle \ , \tag{5.8}$$

and plot in Fig. 5.7 the projection coefficients $c_i = |\langle\tilde{\mathbf{u}}_i|\mathbf{u}\left(\mathbf{r},0\right)\rangle|$ versus the eigen-

TABLE 5.1: Calculated cos-like pseudo-SAW frequencies outlined in the projection of the initial nanostripes' impulsive displacement on the eigenmodes of the phononic crystal [see Fig. 5.7].

Stripes $d = 320$ nm	ν_{1H}	ν_{2H}	ν_{3H}
ν (GHz)	4.61	8.56	12.36
τ (ns)	2.53	2.35	~ 0.65

modes frequency ν_i. As reported in Table 5.1, it is clear that the more weighting modes in the reconstruction of the initial displacement are actually the cos-like pseudo-SAWs, both the fundamental (1H) solution at $\nu_{1H} = 4.61$ GHz and the second harmonic (2H) at $\nu_{2H} = 8.56$ GHz, identified by means of the SAW-likeness coefficient. A third weak contribution at $\nu_{3H} = 12.36$ GHz is ascribed to the third harmonic (3H) pseudosurface wave, the displayed larger broadening being a signature of its stronger coupling to bulk modes [see Section 3.5]. We remark that the numerical simulation's accuracy and reliability, influencing the quality of the 2H projection and of projections on higher harmonics, are severely limited by the mesh refinement and consequently by the calculation power of the workstation running the finite-elements analysis software.

A Fano lineshape is ascribed to both the 1H and 2H distributions standing out in the projection plot. The Fano profile is the general fingerprint of an absorption lineshape occurring when one or more discrete levels interact with a continuum of states, both connected to a ground state [96]. The remarkable feature is the occurrence of peculiar asymmetric and window lineshapes, generated by the configuration interaction (mixing) between the discrete and continuum states. Picturing this definition on the interpretation of our results, as signature of the interaction between the discrete silicon surface wave eigenmode and the continuum of bulk modes, induced in the composite system by the surface stress at the

nanostripe/substrate interface, we adopt the Fano function to fit our asymmetric data sets,

$$F(\nu) = F_0 + A\frac{\left(q\frac{\Gamma}{2} + (\nu - \nu_0)^2\right)}{(\nu - \nu_0)^2 + \left(\frac{\Gamma}{2}\right)^2}\,, \tag{5.9}$$

where the profile index q carries information on the configuration interaction and Γ is the line broadening parameter; ν_0 and F_0 are the fit x and y offsets, respectively, and A is a constant. In order to clarify the meaning of Eq. 5.9, we recall that in the limit case of $q \to \infty$, that is when only the discrete state is connected to the ground state, the above equation describes a symmetric Lorentzian curve with broadening parameter Γ [97].

Thus, a direct evaluation of the linewidth γ of the pseudosurface oscillations is drawn from the curve fit broadening parameter Γ and it is reported in Fig. 5.7. The oscillation lifetimes are reported in Table 5.1. The value for τ_{1H} is validated in terms of its consistency with results for comparable composite systems reported in Ref. [23]. An approximated evaluation of the lifetime of the 3H pseudo-SAW in terms of the same Fano curve fitting procedure returns $\tau_{3H} \sim 650$ ps, giving a hint of its highly damped dynamics.

These results confirm the validity of our interpretation, unambiguously demonstrating that the impulsive heating of the periodic metallic nanostructures launches collective modes mainly localized on the surface of the silicon substrate, which are identified as pseudosurface acoustic waves.

5.5 Extension to the 3D case

The thermomechanical time-dependent model is here extended to the 3D case, with the aim of reproducing the physics of a surface phononic crystal geometry, consisting of metallic nanodisks on silicon, excited by a laser pulse, and to benchmark our results against those from time-resolved diffraction measurements performed

by Giannetti et al. on similar composite systems [1]. In this sense, the measurements give the direct evidence of the detection of surface oscillations launched in a surface-based phononic crystal by means of ultrashort laser pulses, and the theoretical frame here developed aims to explain such physical evidence in terms of a process of excitation of pseudo-SAWs by means of an impulsive thermal expansion of the periodic nanostructures.

We assume the system to be an elastic continuum composed of an array of periodic metallic nanodisks deposited on a silicon substrate. In Fig. 5.8(a), we consider the general configuration where an elastic isotropic nickel nanodisk of diameter d and height $h = 50$ nm is deposited on a crystalline silicon substrate cell, with the canonical periodic boundary conditions set on the sides to reproduce the entire phononic crystal. In this case the height of the silicon cell is reduced to 20 μm, a value exclusively tailored to deal with the higher numerical complexity of a finite elements analysis in three dimensions, still maintaining a sufficient density of eigenstates for the composite system [see Section 3.2]. The array has periodicity $\lambda = 1$ μm, thus ensuring pseudo-SAWs in the hypersonic range. Calculations are performed for $d = 320$ nm [as in Fig. 5.8(a)] and $d = 785$ nm, thus matching the dimensions of the samples experimentally investigated in Ref. [1].

As for the 2D case, by evaluating the laser energy density absorbed respectively by the nanostructures and the substrate, and the specific heat of both Ni and Si, we can estimate that within 10 ps, the temperature of the metallic nanodisks is homogeneously increased by $\Delta T \sim 8$ K, whereas the substrate temperature is essentially unvaried due to the different penetration depth of the 800 nm radiation. The impulsive temperature mismatch ΔT triggers a non-equilibrium expansion of the nanostructures governed by Eq. 5.2. The symmetric total displacement profile of the expanded nanodisk at $t = 10$ ps is presented in Fig. 5.8(b).

The developed theoretical frame involving the projection of the initial impulsive displacement on the calculated eigenmodes of the system is well suited in this 3D case to describe the pseudosurface acoustic waves generation process

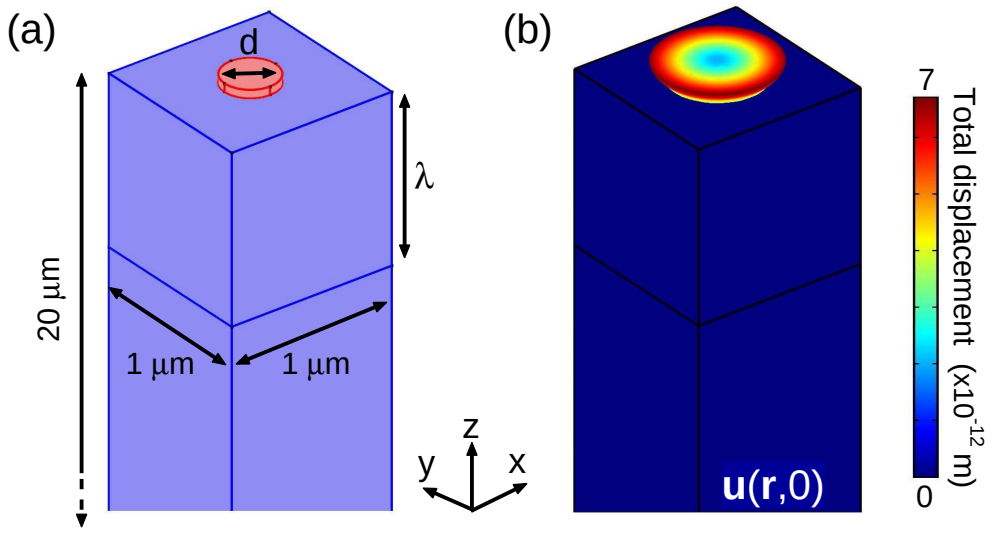

FIGURE 5.8: (a) Simulation cell geometry: general configuration of an elastic isotropic nickel nanodisk of diameter d and height $h = 50$ nm deposited on a crystalline anisotropic silicon substrate cell of height 20 μm. (b) Total displacement profile of the expanded nanodisk calculated at $t = 10$ ps.

and to evaluate the lifetime of these oscillations. On this basis, we solve the elastic eigenvalue problem depicted in Eq. 5.3 via finite element calculations and individuate the launched pseudo-SAW solutions among the eigenmodes of the system by means of the SAW-likeness coefficient. At the same time, considering the nanodisks' symmetric initial displacement, we discriminate between sin-like and cos-like pseudo-SAWs in terms of their contribution to the initial impulsive thermal expansion in the projection at $t = 10$ ps, practically showing that only the cos-like oscillations (even symmetry) are launched by the impulsive expansion. Following Eq. 5.8, these evidences are clear in the plots of the projection coefficients $c_i = |\langle \tilde{\mathbf{u}}_i | \mathbf{u}(\mathbf{r}, 0) \rangle|$ for the 3D problem, reported versus the eigenfrequencies ν_i in Fig. 5.9.

More in details, in the non-trivial analysis of the projection plot of Fig. 5.9(a) for the phononic crystal configuration with nanodisks of diameter $d = 320$ nm, we gather complete information on the mechanical response of the composite system

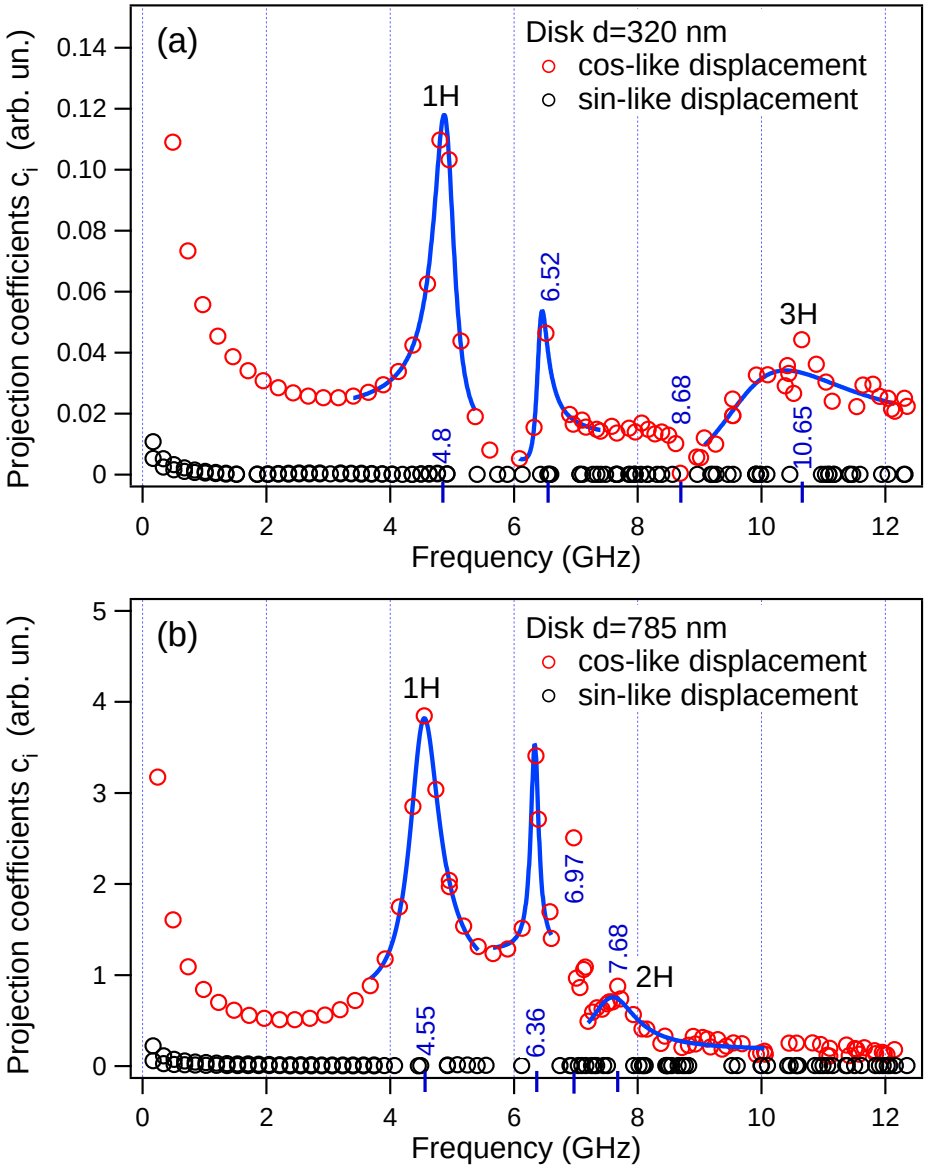

FIGURE 5.9: Projections (3D) of the initial thermal expansion displacement on the eigenmodes of the composite system, with cos-like (red circles) and sin-like (black circles) displacement symmetry. Here reported are the results of simulations performed for phononic crystals with nanodisk diameter of, respectively, (a) $d = 320$ nm and (b) $d = 785$ nm. The calculated curves with cos-like displacement symmetry are fitted with the Fano function described in Eq. 5.9 (blue line).

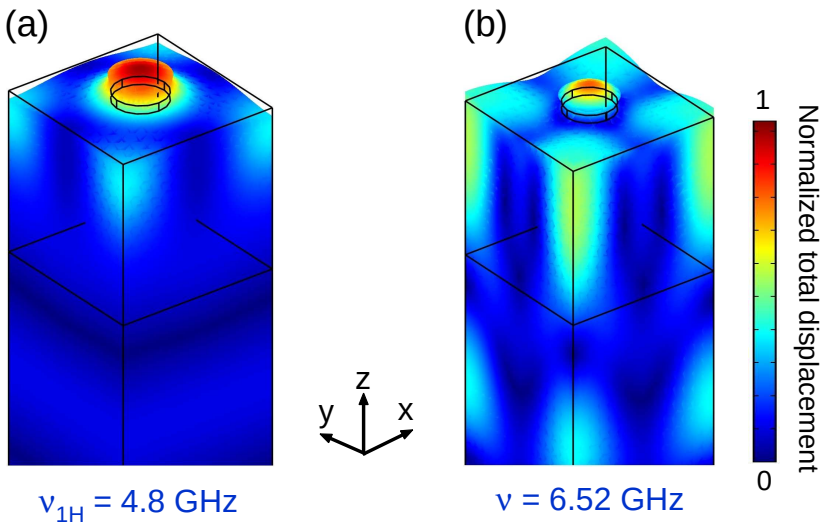

FIGURE 5.10: Normalized total displacement of (a) the fundamental $\nu_{1H} = 4.8$ GHz cos-like pseudo-SAW and (b) the $\nu = 6.52$ GHz cos-like surface mode, solutions of the 3D acoustic eigenvalue problem for the $d = 320$ nm phononic crystal configuration.

to the impulsive thermal excitation of the surface nanostructures. We identify the fundamental excited pseudo-SAW at the frequency $\nu_{1H} = 4.8$ GHz as the more weighting contribution in the projection to the system oscillation dynamics. The line profile of the fundamental pseudo-SAW has a clear Fano appearance, highlighting the interaction between the discrete silicon surface wave eigenmode and the continuum of bulk modes, induced in the composite system by the surface stress at the nanostructure/substrate interface. We make use of Eq. 5.9 to fit the 1H line profile and calculate its broadening parameter for an immediate evaluation of the curve's linewidth $\gamma_{1H} = 0.406$ ns^{-1}. As reported in Table 5.2, we note from the plot that an additional surface component at 6.52 GHz enters this 3D projection as a weak contributing term to the initial nanodisks expansion. The analysis of the eigenmodes displacement profiles, reported in Fig. 5.10, shows similarities between the fundamental pseudo-SAW and the symmetric surface oscillation of the 6.52 GHz eigenmode, but on the other hand it unambiguously evidences a

TABLE 5.2: Calculated cos-like pseudo-SAW frequencies outlined in the projection of the initial nanodisks' impulsive displacement on the eigenmodes of the phononic crystals [see Fig. 5.9].

Disks $d = 320$ nm	ν_{1H}		ν_{2H}	ν_{3H}
ν (GHz)	4.8	6.52	(8.69)	10.65
τ (ns)	2.46			0.425
Disks $d = 785$ nm	ν_{1H}			ν_{2H}
ν (GHz)	4.55	6.36	6.97	7.68
τ (ns)	1.7	(~ 6.0)		1.11

non-negligible bulk-like component, thus leading to its classification as bulk mode with a secondary surface-like contribution.

Surprisingly, in the study of higher frequency features, we are not able to clearly individuate a second harmonic pseudosurface oscillation signature in the projection plot. A profile centered at 10.65 GHz is observed, with a lower but non-negligible contribution to the initial impulsive thermal expansion, and due to its large broadening and surface displacement profile it is addressed, similarly to the 2D case, as the third harmonic (3H) highly damped pseudosurface feature. The 3H component's larger linewidth $\gamma_{3H} = 2.35$ ns^{-1} (from the Fano curve fit) is in agreement with the stronger surface confinement for higher harmonics and the greater mechanical damping in terms of elastic energy radiation to bulk modes, as described in Refs. [23, 1].

Accordingly to the discussion and results for the 2D case, we expect that the nanodisks' impulsive expansion would excite a 2H pseudo-SAW, but the result of the simulations denies us. To find an answer to this issue we take in consideration the (u_x, u_y, u_z) components of the eigenvalue displacement $\mathbf{u}_i$ and separately project the initial displacement $\mathbf{u}(\mathbf{r}, 0)$ on the single component, as shown

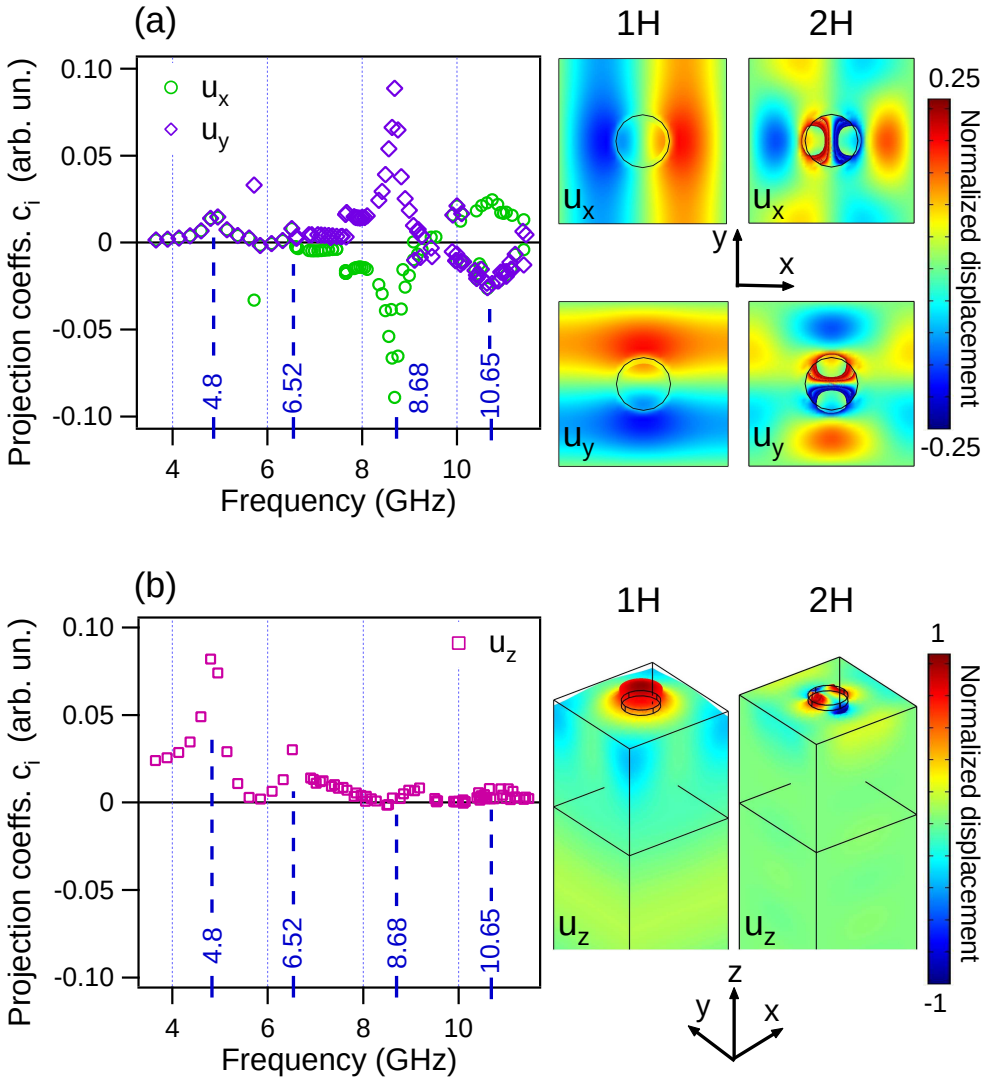

FIGURE 5.11: Projections (Left) of the initial nanodisk's displacement on the (a) u_x, u_y, and (b) u_z eigenvalues' displacement components for the $d = 320$ nm phononic crystal configuration, with the corresponding 1H and 2H displacements reported (Right).

in Fig. 5.11. Pointing our attention to the higher harmonics frequency range, in Fig. 5.11(b) we can confirm that the projection on the u_z transversal displacement component is approximately null, while on the other hand, in Fig. 5.11(a) the projections on the u_x and u_y in-plane longitudinal components are totally similar to

the 2D projection reported in Fig. 5.7, with neath 2H contributions at 8.69 GHz. The fact that such contributions are not present in the general projection [Eq. 5.8] is explained by their projection profiles, which are equal (for symmetry) but opposite in sign, leading to a zero in their summation. Physically, this translates in terms of the 2H displacement profile in having the u_x and u_y components equal in modulus but opposite in phase, as we see in Fig. 5.11(a), thus not matching the totally symmetric initial surface nanodisk expansion condition [see Fig. 5.8(b)] and explaining why the impulsive displacement at $t = 10$ ps does not excite a 2H pseudosurface acoustic wave.

Our calculations are benchmarked against time-resolved optical diffraction measurements performed on the same composite systems [1]. The experimental results are here reported in Fig. 5.12, in a wavelet analysis framework. By definition, the wavelet directly shows the frequency content of the measured diffracted signal $\Delta R/R$ within time windows, thus carrying information on both measured surface oscillations' frequency components and lifetimes. The theoretical outcome reproduces the main experimental features. In the case of $d = 320$ nm in Fig. 5.12(a), the calculated pseudo-SAW frequencies match the diffracted signal's frequency components at zero delay. This is achieved introducing a correction factor in the modulus of the elastic stiffness tensor c_{ijmn}, entering the acoustic equation of motion [Eq. 5.1]. This correction is due to the increased strain originated by both the periodic nanostructures mass loading on the silicon substrate and the lattice mismatch at the nickel/silicon interface. This correction factor is taken into account in terms of an increased effective elastic stiffness tensor, as formerly discussed in Ref. [98]. The need to adopt a greater correction factor for the larger nanodisk configuration is a further confirmation of the validity of our thermomechanical model. The numerically evaluated fundamental pseudosurface wave lifetime $\tau_{1H} = 1/\gamma_{1H} = 2.46$ ns well fits with the wavelet displayed damping of the signal's 4.8 GHz frequency component. In the same way, the expected shorter lifetime $\tau_{3H} = 1/\gamma_{3H} = 425 \pm 160$ ps of the 3H pseudo-SAW satisfactorily enters

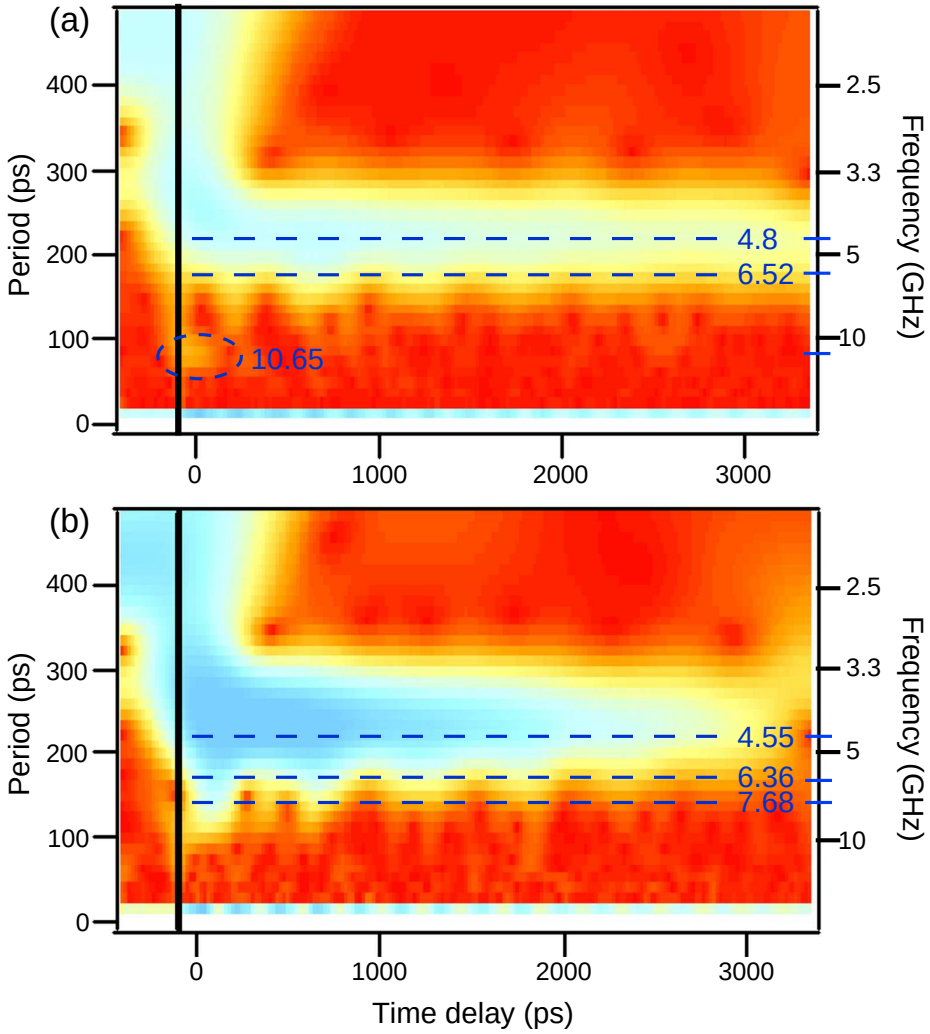

FIGURE 5.12: 3D Wavelet analysis of the time-resolved diffraction measurements. Here reported (inverted color scale) are the experimental results collected for phononic crystals with nanodisk diameter of, respectively, (a) $d = 320$ nm and (b) $d = 785$ nm. The calculated pseudo-SAW frequencies are evidenced in blue.

(considering the prominent numerical error) the shorter time range of the corresponding 250 ps experimental counterpart, observable as a small signature in the wavelet plot. Moreover, the additional bulk mode with a secondary surface component observed in the projection at $\nu = 6.52$ GHz, even if not directly visible because covered by the stronger 1H signal, still has a clear fingerprint in the

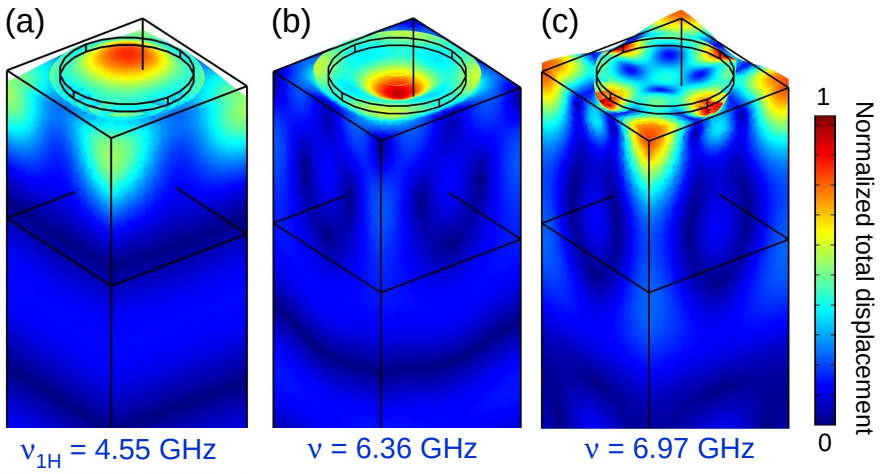

FIGURE 5.13: Normalized total displacement of (a) the fundamental $\nu_{1H} = 4.55$ GHz cos-like pseudo-SAW, and the (b) $\nu = 6.36$ GHz, (c) $\nu = 6.97$ GHz cos-like surface modes, solutions of the 3D acoustic eigenvalue problem for the $d = 785$ nm phononic crystal configuration.

wavelet plot in terms of a frequency beating visible in the signal on longer delays, suggesting that its contribution to the surface oscillation is effectively translated in a variation of the diffracted signal, thus being optically detected.

The additional weak surface term also appears when performing the same analysis on the thermomechanical simulations results for the $d = 785$ nm phononic crystal configuration. As summarized in Table 5.2, in the projections plot of Fig. 5.9(b), the 1H and 2H excited pseudo-SAW are found at $\nu_{1H} = 4.55$ GHz and $\nu_{2H} = 7.68$ GHz, respectively, and the third contribution is distinguishable at 6.36 GHz. Comparing these evidences with the experimental results reported in Fig. 5.12(b), the wavelet unambiguously displays the signature of the 1H and 2H (here observable) pseudosurface oscillations at zero delay. The eigenfrequencies are correctly downshifted, accounting for the increased mass loading of the system due to the larger filling fraction, as discussed in Section 3.3. Also in this case, the surface oscillation at 6.36 GHz, not directly visible in the wavelet because covered by the stronger 1H signal, still sets up a clear frequency beating, with the fundamental pseudo-SAW, visible in the signal on longer delays. Its contribution to the

surface oscillation is thus effectively optically detected. A further confirmation is given by the analysis of the surface displacement of this eigenmode, as reported in Figs. 5.13(a) and 5.13(b), showing a profile very similar to the fundamental's, with a stronger oscillation confinement in the nanostructure and a weak energy radiation component in the bulk. Concerning the pseudosurface oscillations' lifetimes calculated by means of the Fano profile curve fitting procedure, if the second harmonic $\tau_{2H} = 1/\gamma_{2H} = 1.11$ ns overestimates the reported experimental result, the fundamental $\tau_{1H} = 1/\gamma_{1H} = 1.7$ ns fits with some approximations to the measured damping displayed in the wavelet. We finally point out that the small broadening of the 6.36 GHz surface component, leading to a not physical 6.0 ± 1.5 ns lifetime, is corrupted by the lack of calculated solutions in that frequency range, and that the isolated feature in the projection at 6.97 GHz corresponds to a bulk modes with a non-negligible surface oscillation component, clearly observable in terms of the surface displacement analysis reported in Fig. 5.13(c), but hard to individuate in the measured signal.

5.6 Summary

In conclusion, presented in this Chapter is a theoretical framework allowing to properly investigate the thermomechanics of hypersonic surface phononic crystals excited by ultrafast laser pulses. Exploiting finite-elements analysis, we followed step by step in the time domain the initial impulsive heat-driven displacement. The 3D thermomechanical time-dependent model demonstrates without doubts that hypersonic pseudosurface acoustic waves are optically excited. The lifetimes of the generated pseudo-SAWs are evaluated. The benchmark of the outcomes of our calculations, against experimental results from time-resolved infrared diffraction measurements, verifies that the theoretical framework well reproduces the main experimental features. These results give credence to the full thermomechanical

model as a unique tool to understand the physics of hypersonic surface phononic crystals.

Chapter 6

Conclusions

In this thesis, we presented a theoretical framework allowing to investigate the thermomechanics of hypersonic phononic crystals triggered by ultrafast laser pulses. Analyzing the detailed mechanisms behind the optical generation of pseudosurface acoustic waves, we addressed the full thermomechanical problem and identified pseudo-SAW solutions [45]. In a realistic physical scenario, there is no distinction between the eigenmodes of nanostructures and SAWs, the solution of the elastic equation being a pseudo-SAW partially localized on the nanostructures and radiating energy into the bulk. Pursuing a strategy that can be applied to any surface phononic crystal, we investigated pseudo-SAW line shapes, gap opening and mechanical energy scattering beyond a perturbative approach.

We made use of the outlined theoretical framework in the case of a hypersonic surface phononic crystal made of periodic nickel stripe on a silicon substrate, investigating the pseudosurface acoustic wave frequency gap over the entire filling fraction range, starting from the case where the periodic nanostructures act as a perturbation, to finally reach the substrate full coverage. A preliminary understanding of how the construction parameters affect the frequency gap has been achieved. We showed that the pseudo-SAW frequency gap results from a combination of geometry $\{p, h\}$ and mass loading $\{m, \rho\}$ factors, the two affecting the

pseudo-SAW frequencies in opposite ways. A trade-off between p and m is thus necessary for tailoring the pseudo-SAW frequencies or frequency gap for the application at hand. The mechanical energy spatial distribution of pseudo-SAW as a function of the filling fraction has been studied, potentially allowing to tailor the device's parameters in order to minimize the energy content scattered out of the desired modes.

Exploiting finite-elements analysis to study the impulsive generation and lifetime of pseudo-SAWs in these nanostructured composite systems, we modeled ab-initio the thermal expansion dynamics induced by ultrashort laser pulses. In the ultrafast nanocalorimetry perspective, we reported the break-down of thermodynamical equilibrium between electrons and phonons on the ns time scale at ~ 10 K, at a temperature two order of magnitudes higher than that observed in standard transport measurements. These findings set the limits of applicability of ultrafast nanocalorimetry well above liquid He temperature, the electron-phonon temperature decoupling preventing a proper definition of the temperature concept of the nanosample as a whole. In this sense, the present work, while making available a proper tool for interpreting all-optical time-resolved nanocalorimetry experiments, suggests a new route for investigating the physics of the electron-phonon decoupling where the sub-Kelvin temperature requirement is substituted by the ns time resolution.

Combining the initial condition for the generation of surface acoustic oscillations, given by the system's thermal expansion dynamics, with the developed full mechanical model, we were able to follow step by step in the time domain the initial impulsive heat-driven displacement launching pseudo-SAWs and to evaluate their lifetime. The results demonstrated without doubts that hypersonic pseudosurface acoustic waves are optically excited in surface phononic crystals by the nanostructures' impulsive thermal expansion. As a successful benchmark, the simulations outcomes were compared, in terms of a wavelet analysis framework, with time-resolved optical diffraction measurements performed on the same composite

systems by Giannetti et al. [1]. This evidence gives credence to our theoretical framework as a unique tool to understand the detailed thermomechanics of hypersonic phononic crystals, opening to the possibility of optically control the excitation of hypersonic pseudo-SAWs and thermal gradients in arrays of metallic nanostructures on substrate.

Bibliography

[1] C. Giannetti *et al.*, Phys. Rev. B **76**, 125413 (2007).

[2] H. J. Maris, Scientific American **278**, 86 (1998).

[3] C. Thomsen, H. T. Grahn, H. J. Maris, and J. Tauc, Phys. Rev. B **34**, 4129 (1986).

[4] E. Morozov, Y. Laamiri, P. Ruello, D. Mounier, and V. Gusev, Eur. Phys. J. Special Topics **153**, 239 (2008).

[5] M. I. Kaganov, I. M. Lifshitz, and L. V. Tanatarov, Sov. Phys. JEPT **4**, 173 (1957).

[6] J. A. Rogers, A. A. Maznev, M. J. Banet, and K. A. Nelson, Annu. Rev. Mater. Sci. **30**, 117 (2000).

[7] T. Pezeril, F. Leon, D. Chateigner, S. Kooi, and K. A. Nelson, Appl. Phys. Lett. **92**, 061908 (2008).

[8] H.-Y. Hao and H. J. Maris, Phys. Rev. B **64**, 064302 (2001).

[9] A. V. Scherbakov, P. J. S. van Capel, A. V. Akimov, J. I. Dijkhuis, D. R. Yakovlev, T. Berstermann, and M. Bayer, Phys. Rev. Lett. **99**, 057402 (2007).

[10] L. D. Landau and E. M. Lifshitz, *Theory of Elasticity* (Butterworth-Heinemann, Oxford, 1986).

[11] M. Cecchini, V. Piazza, F. Beltram, D. G. Gevaux, M. B. Ward, A. J. Shields, H. E. Beere, and D. A. Ritchie, Appl. Phys. Lett. **86**, 241107 (2005).

[12] M. Cecchini, V. Piazza, G. D. Simoni, F. Beltram, H. E. Beere, and D. A. Ritchie, Appl. Phys. Lett. **88**, 212101 (2006).

[13] M. M. de Lima, R. Hey, P. V. Santos, and A. Cantarero, Phys. Rev. Lett. **94**, 126805 (2005).

[14] M. M. de Lima, M. van der Poel, P. V. Santos, and J. M. Hvam, Phys. Rev. Lett. **97**, 045501 (2006).

[15] J. Rudolph, R. Hey, and P. V. Santos, Phys. Rev. Lett. **99**, 047602 (2007).

[16] Y. Sugawara, O. B. Wright, O. Matsuda, M. Takigahira, Y. Tanaka, S. Tamura, and V. E. Gusev, Phys. Rev. Lett. **88**, 185504 (2002).

[17] T. Tachizaki, T. Muroya, O. Matsuda, Y. Sugawara, D. H. Hurley, and O. B. Wright, Rev. Sci. Instrum. **77**, 043713 (2006).

[18] D. H. Hurley, O. B. Wright, O. Matsuda, T. Suzuki, S. Tamura, and Y. Sugawara, Phys. Rev. B **73**, 125403 (2006).

[19] D. M. Profunser, O. B. Wright, and O. Matsuda, Phys. Rev. Lett. **97**, 055502 (2006).

[20] A. A. Maznev, Elsevier Ultrasonics **49**, 1 (2009).

[21] A. Bartels, T. Dekorsy, and H. Kurz, Phys. Rev. Lett. **82**, 1044 (1999).

[22] A. Huynh, N. D. Lanzillotti-Kimura, B. Jusserand, B. Perrin, A. Fainstein, M. F. Pascual-Winter, E. Peronne, and A. Lemaître, Phys. Rev. Lett. **97**, 115502 (2006).

[23] H.-N. Lin, H. J. Maris, L. B. Freund, K. Y. Lee, H. Luhn, and D. P. Kern, J. Appl. Phys. **73**, 37 (1993).

[24] M. Nisoli, S. D. Silvestri, A. Cavalleri, A. M. Malvezzi, A. Stella, G. Lanzani, P. Cheyssac, and R. Kofman, Phys. Rev. B **55**, (1997).

[25] N. D. Fatti, C. Voisin, F. Chevy, F. Vallée, and C. Flytzanis, J. Chem. Phys. **110**, 11484 (1999).

[26] J. Burgin *et al.*, Nano Lett. **8**, 1296 (2008).

[27] W. Huang, W. Qian, and M. A. El-Sayed, Nano Lett. **4**, 1741 (2004).

[28] W. Huang, W. Qian, and M. A. El-Sayed, J. Phys. Chem. B **109**, 18881 (2005).

[29] R. Taubert, F. Hudert, A. Bartels, F. Merkt, A. Habenicht, P. Leiderer, and T. Dekorsy, New J. Phys. **9**, 376 (2007).

[30] J. Burgin, P. Langot, N. D. Fatti, F. Vallée, W. Huang, and M. A. El-Sayed, J. Phys. Chem. C **112**, 11231 (2008).

[31] A. Arbouet, N. D. Fatti, and F. Vallée, J. Chem. Phys. **124**, 144701 (2006).

[32] P. Billaud *et al.*, J. Phys. Chem. C **112**, 978 (2008).

[33] R. J. Stoner and H. J. Maris, Phys. Rev. B **48**, 16373 (1993).

[34] B. C. Gundrum, D. G. Cahill, and R. S. Averback, Phys. Rev. B **72**, 245426 (2005).

[35] H.-K. Lyeo and D. G. Cahill, Phys. Rev. B **73**, 144301 (2006).

[36] M. Highland, B. C. Gundrum, Y. K. Koh, R. S. Averback, D. G. Cahill, V. C. Elarde, J. J. Coleman, D. A. Walko, and E. C. Landahl, Phys. Rev. B **76**, 075337 (2007).

[37] R. J. von Gutfeld and A. H. Nethercot, Phys. Rev. Lett. **17**, 868 (1966).

[38] B. Perrin, E. Péronne, and L. Belliard, Elsevier Ultrasonics **44**, (2006).

[39] C. Voisin, N. D. Fatti, D. Christofilos, and F. Vallée, Appl. Surface Science **164**, 131 (2000).

[40] D. H. Hurley and K. L. Telschow, Phys. Rev. B **66**, 153301 (2002).

[41] J.-F. Robillard, A. Devos, and I. Roch-Jeune, Phys. Rev. B **76**, 092301 (2007).

[42] D. H. Hurley, R. Lewis, O. B. Wright, and O. Matsuda, Appl. Phys. Lett. **93**, 113101 (2008).

[43] W. Chao, B. D. Harteneck, J. A. Liddle, E. H. Anderson, and D. T. Attwood, Nature **435**, 1210 (2005).

[44] M. E. Siemens, Q. Li, M. M. Murnane, H. C. Kapteyn, R. Yang, E. H. Anderson, and K. A. Nelson, Appl. Phys. Lett. **94**, 093103 (2009).

[45] D. Nardi, F. Banfi, C. Giannetti, B. Revaz, G. Ferrini, and F. Parmigiani, Phys. Rev. B **80**, 104119 (2009).

[46] L. Esaki and R. Tsu, IBM J. Res. Dev. **14**, 61 (1970).

[47] J. C. Knight, J. Broeng, T. A. Birks, and P. S. J. Russell, Science **282**, 1476 (1998).

[48] P. S. J. Russell, Science **299**, 358 (2003).

[49] E. Yablonovitch, Phys. Rev. Lett. **58**, 2059 (1987).

[50] S. John, Phys. Rev. Lett. **58**, 2486 (1987).

[51] T. F. Krauss, R. M. D. L. Rue, and S. Brand, Nature **383**, 699 (1996).

[52] M. S. Kushwaha, P. Halevi, G. Martínez, L. Dobrzynski, and B. Djafari-Rouhani, Phys. Rev. B **49**, 2313 (1994).

[53] Y. Tanaka and S. I. Tamura, Phys. Rev. B **58**, 7958 (1998).

[54] Y. Tanaka and S. I. Tamura, Phys. Rev. B **60**, 13294 (1999).

[55] H. A. Haus, IEEE Trans. Sonics Ultrason. 259 (1977).

[56] D.-P. Chen and H. A. Haus, IEEE Trans. Sonics Ultrason. 395 (1985).

[57] S. Datta and B. J. Hunsinger, J. Appl. Phys. **50**, 5661 (1979).

[58] H. Robinson, Y. Hahn, and J. N. Gau, J. Appl. Phys. **65**, 4573 (1989).

[59] J. R. Dutcher, S. Lee, B. Hillebrands, G. J. McLaughlin, B. G. Nickel, and G. I. Stegeman, Phys. Rev. Lett. **68**, 2464 (1992).

[60] A. A. Maznev and O. B. Wright, J. Appl. Phys. **105**, 123530 (2009).

[61] N. E. Glass and A. A. Maradudin, J. Appl. Phys. **54**, 796 (1983).

[62] X. Zhang, T. Jackson, E. Lafond, P. Deymier, and J. Vasseur, Appl. Phys. Lett. **88**, 041911 (2006).

[63] B. Bonello, C. Charles, and F. Ganot, Appl. Phys. Lett. **90**, 021909 (2007).

[64] R. Sainidou and N. Stefanou, Phys. Rev. B **73**, 184301 (2006).

[65] F. Liu, F. Cai, Y. Ding, and Z. Liua, Appl. Phys. Lett. **92**, 103504 (2008).

[66] B. Morvan, A. C. Hladky-Hennion, D. Leduc, and J. L. Izbicki, J. Appl. Phys. **101**, 114906 (2007).

[67] B. Auld, *Acoustic Fields and Waves in Solids, Vol.II* (Krieger Publ., Malabar, FL, 1990).

[68] W. Cheng, J. Wang, U. Jonas, G. Fytas, and N. Stefanou, Nature Materials **5**, 830 (2006).

[69] COMSOL Multiphysics finite element software, Version 3.5a (3.5.0.608), COMSOL AB, Sweden.

[70] A. Okhotin, A. Pushkarskii, and V. Gorbachev, *Thermophysical Properties of Semiconductors* (Atom Publ. House, Moscow, 1972).

[71] Davies and Associates, *14ASM Metal Handbook, 10th ed.* (ASM International, Metals Park, 1996).

[72] S. Hufner, *Photoelectron Spectroscopy* (Springer, Berlin-Heidelberg, 2003).

[73] D. Courjon, *Near-field microscopy and near-field optics* (Springer, Berlin, 2004).

[74] G. A. Antonelli, H. J. Maris, S. G. Malhotra, and J. M. E. Harper, J. Appl. Phys. **91**, 3261 (2002).

[75] G. Cahill, W. K. Ford, K. E. Goodson, G. D. Mahan, A. Majumdar, H. J. Maris, R. Merlin, and S. R. Phillpot, J. Appl. Phys. **93**, 793 (2003).

[76] V. Juvé, M. Scardamaglia, P. Maioli, A. Crut, S. Merabia, L. Joly, N. D. Fatti, and F. Vallée, Phys. Rev. B **80**, 195406 (2009).

[77] K. Schwab, E. A. Henriksen, J. M. Worlock, and M. L. Roukes, Nature **404**, 974 (2000).

[78] F. Giazotto, T. T. Heikki, A. Luukanen, A. M. Savin, and J. P. Pekola, Rev. Mod. Phys. **78**, 217 (2006).

[79] W. C. Fon, K. C. Schwab, J. M. Worlock, and M. L. Roukes, Nano Lett. **5**, 1968 (2005).

[80] C. Giannetti, F. Banfi, D. Nardi, G. Ferrini, and F. Parmigiani, IEEE Photonics Journal **1**, 21 (2009).

[81] C. Senatore, *Specific heat measurement on industrial superconductors* (Invited talk, Brescia, 28^{th} April 2006).

[82] P. B. Johnson and R. W. Christy, Phys. Rev. B **9**, 5056 (1974).

[83] Landolt-Börnstein, *New Series III/15C* (Oxford University Press, Oxford, 2002).

[84] M. N. Özişik, *Heat Conduction, II Ed.* (Wiley-Interscience, Malabar, FL, 1993).

[85] D. A. Young and H. J. Maris, Phys. Rev. B **40**, 3685 (1989).

[86] E. D. Swartz and R. O. Pohl, Rev. Mod. Phys. **61**, 605 (1989).

[87] When working at or below liquid He temperatures, repetition rate ~ 1 MHz or less needs to be used in order for the average temperatures in proximity of the nanodisk interface to remain close to the one imposed by the cryostate.

[88] $C_{el} = \gamma_{el} \cdot T_{el}$ with $\gamma_{el} = 1.065 \cdot 10^3$ $\mathrm{Jm^{-3}K^3}$ taken from P. B. Allen, Phys. Rev. B **36**, 2920 (1987), C_{ph} is calculated with PCWS, C_{Si} is derived from the Debye Model, k_{el} and k_{ph} are taken from C. Y. Ho et al., J. Phys. Chem. Ref. Data **7**, 959 (1978), k_{Si} is taken from Glassbrenner et al., Phys. Rev. **134**, A1058 (1964).

[89] P. B. Allen, Phys. Rev. Lett. **59**, 1460 (1987).

[90] The function $\alpha^2 F$ and the DOS for Cu have been calculated implementing the code PWscf part of the Quantum ESPRESSO program.

[91] P. B. Allen, Phys. Rev. B **36**, 2920 (1987).

[92] S. D. Brorson, A. Kazeroonian, J. S. Moodera, D. W. Face, T. K. Cheng, E. P. Ippen, M. S. Dresselhaus, and G. Dresselhaus, Phys. Rev. Lett. **64**, 2172 (1990).

[93] H. E. Elsayed-Ali, T. B. Norris, M. A. Pessot, and G. A. Mourou, Phys. Rev. Lett. **58**, 1212 (1987).

[94] E. T. Swartz and R. O. Pohl, Appl. Phys. Lett. **51**, 2200 (1987).

[95] M. L. Roukes, M. R. Freeman, R. S. Germain, R. C. Richardson, and M. B. Ketchen, Phys. Rev. Lett. **55**, 422 (1985).

[96] U. Fano, Phys. Rev. **124**, 1866 (1961).

[97] G. Grosso and G. P. Parravicini, *Solid State Physics* (Academic Press, San Diego, CA, 2000).

[98] R. Zhu, E. Pan, P. W. Chung, X. Cai, K. M. Liew, and A. Buldum, Semicond. Sci. Technol. **21**, 906 (2006).